ENGINEERING SCIENCE AND TECHNOLOGY

Seed Money Fund

Investigation of a Novel Technique for Infrared Energy Detection and Imaging

K. Korsah,[1] R. A. Kisner,[1] L. A. Boatner,[2] and H. M. Christen[2]
[1]*Engineering Science and Technology Division*
[2]*Condensed Matter Science Division*

This project focused on the investigation of a new piezoelectric material for its suitability as a thermal detector using surface acoustic wave (SAW) technology. The long-term goal is to use the technology for infrared (IR) detection and imaging.

Thermal (IR) imaging remains a cornerstone technology for many military applications, including small unit operations, ground, air and sea target acquisition, missile seekers, and threat warning. However, the cost of present-day high-performance cameras can range between $70K and $170K. Besides cost, another disadvantage of these systems is that they typically are required to be cryogenically cooled. Therefore, there is a need for the development of more sensitive, uncooled, and less costly thermal imaging devices for these as well as other (civilian) applications. The continued need for improved IR imaging systems is evidenced by the statement in June 2001 by Dr. Tony Tether, Director of the Defense Advanced Research Projects Agency (DARPA), before the subcommittee on Military Research and Development, that the program began funding the investigation of new concepts for thermally sensitive microstructures in FY 2000.

The immediate, expected result of this project was a single-pixel surface acoustic wave (SAW) infrared detector. The long-term goal of the project is to use the results obtained under this project as a basis for further research and development of an uncooled IR detector camera, based on SAW technology that can be purchased for around $1000 or less. This would be a unique instrument and would revolutionize the IR camera market in much the same way as the development of the uncooled microbolometer camera has over the last several years. Low cost is the key that opens the door to hundreds of markets.

Introduction

The traditional application of SAW technology has been in communications and, more recently, in sensor applications. SAW application in IR imaging has not been explored to any extent. In almost all traditional applications of SAW sensors, the objective is to have negligible changes in the substrate parameters as a function of temperature. For application as an IR sensor, however, this is the means of transduction, so changes in substrate parameters as a function of temperature must be as high as possible. In fact, many of the requirements for a SAW IR (thermal) sensor are of less significant consideration in the more conventional applications of SAW devices. These requirements include the following: (1) high-temperature coefficient; (2) sensitivity to ~10 mK; (3) temperature changes; (4) small pixel size; (5) low interference from non-SAW modes; (6) robust design; and (6) simple instrumentation.

A SAW device is characterized by the electrical excitation of a surface acoustic wave in a piezoelectric single-crystal plate or substrate (e.g., quartz, lithium niobate).[1, 2] The electrical excitation is produced by means of a metallic (e.g., aluminum) interdigital transducer (IDT) structure. When the SAW is used as a sensor in an oscillator configuration, the influence of the measurand (e.g., gas, temperature/infrared energy) on the acoustic wave phase propagation speed ϑ is used for the sensor effect. In the oscillator configuration, this velocity perturbation gives rise to a frequency shift Δf given by

$$\Delta f = (\partial f/\partial m)\cdot\Delta m + (\partial f/\partial c)\cdot\Delta c + (\partial f/\partial \varepsilon)\cdot\Delta\varepsilon + (\partial f/\partial \sigma)\cdot\Delta\sigma + (\partial f/\partial T)\cdot\Delta T + (\partial f/\partial P)\cdot\Delta P \quad , \qquad (1)$$

where $\Delta\sigma$ and $\Delta\varepsilon$ signify conductivity and dielectric changes, respectively (the changes in σ and ε are due to *acoustoelectric interactions*); Δm and Δc are mass and viscoelastic constant changes, respectively, and are due to *mechanical interactions*; and $\Delta T + \Delta P$ are temperature and pressure changes, respectively. Equation (1) shows that the SAW frequency is sensitive to a number of parameters; however, depending on the type of sensor being developed, it is possible to reduce the effect of other parameters on the frequency. For example, for use as a gas sensor, the surface of the substrate is covered with a chemically active, selective thin film. This film is capable of adsorbing specific molecules. This adsorption gives an increased mass loading of the Raleigh wave. In this case, temperature effects are reduced by using a piezoelectric cut that has a zero temperature coefficient.

If the measurand is infrared energy (temperature), any of the parameters in Eq. (1) that change significantly with temperature will contribute to the output frequency shift. The fifth term $[(\partial f/\partial T)\cdot\Delta T]$ signifies a direct temperature effect of the substrate via the temperature coefficient of delay (TCD) or, as is more popularly referred to, the temperature coefficient of frequency (TCF), given by the following equation

$$TCD = (1/L)*(\partial L/\partial T) - (1/\vartheta)*(\partial\vartheta/\partial T) \quad , \qquad (2)$$

where L is the acoustic path length.[2] However the temperature effect through the TCD is typically small, usually of the order of parts per million. To be a good candidate for IR sensing, we either require a material with a much higher TCD, or one in which other parametric changes have a much greater effect. In our study we investigated potassium tantalum niobate ($KTa_{1-x}Nb_xO_3$), or KTN, as a potential candidate because it exhibits very large changes in dielectric constant as a function of temperature. In particular, KTN exhibits significant permittivity and electro-optic effects at temperatures near the ferroelectric curie point T_c. By adjusting the Ta/Nb ratio, T_c can be varied continuously from –273°C ($x \leq 0.008$) to 435°C (i.e., to the value of T_c for pure $KnbO_3$). For $x \geq 0.05$, T_c has been shown to follow the simple linear relationship given by

$$T_c[°C] = 676°C \cdot x - 241°C \quad . \qquad (3)$$

The dielectric constants as a function of temperature for films grown with different Ta/Nb ratios is shown in Fig. 1. In the figure, curve (a) corresponds to $KNbO_3$, curve (b) corresponds to $KTa_{0.19}Nb_{0.81}O_3$, and curve (c) corresponds to $KTa_{0.25}Nb_{0.75}O_3$.

Technical Approach

The approach taken in this study was to first design and fabricate thin films of KTN of the desired composition, design and fabricate SAW structures using the KTN material as well as lithium niobate ($LiNbO_3$) and compare the temperature response of the two materials. $LiNbO_3$ was used for this comparison because it is one of the more common SAW device materials that possess a relatively large temperature coefficient of frequency (TCF). For example, a SAW device with propagation in the Z direction on Y-cut $LiNbO_3$ (YZ-$LiNbO_3$) has a temperature coefficient of approximately 90 ppm/°C. The temperature coefficient of 128° lithium niobate has a lower temperature coefficient (~75 ppm/°C), but the lower bulk wave interference tends to improve the response (lower distortion) in broad bandwidth devices. If KTN is going to show any promise as a thermal detector in a SAW configuration, it would be important to show that it's much more sensitive to temperature than $LiNbO_3$.

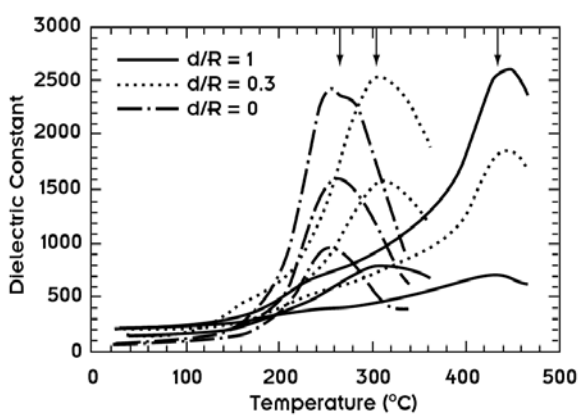

Fig. 1. Dielectric constant as a function of temperature for films grown with different Ta/Nb ratios. By changing the Ta/Nb ratio, it is possible to shift the (steep) slope of the curve to room temperature.

A major challenge was to be able to fabricate sufficiently thick films (several microns) of the KTN material. Eventually, after overcoming several challenges, 0.6 µm thick of $K(Ta_{1-x}Nb_x)O_3$ [x = 0.5] epitaxial films were successfully grown and polished on $KTaO_3$ (001) substrates approximately 1 mm thick. The film was grown after the method of Christen et. al[3] by pulsed laser deposition using a four-target mixing approach (repeated sequential deposition of sub-monolayer amounts of $KTaO_3$ – KNO_3 – $KNbO_3$ – KNO_3 – etc.). KNO_3 is added as an additional K-source to compensate for the volatility of this element. Target firing sequence is in 4-pulse bursts at 100 Hz (248 nm, 200 mJ per pulse), with the target sequence completed once per second.

The perovskite targets were prepared from commercial $KTaO_3$ and $KNbO_3$ powders (Alfa Aesar) by hot-pressing in vacuum at ~1300°C ($KTaO_3$) and 1100°C ($KNbO_3$) and from commercial KNO_3 powder (Alfa Aesar) by cold-pressing at 6000 lb in air after carefully grinding the power to small grain size.

Film characterization by profilometry on a reference sample indicated a thickness of 600 nm for a total of 40,000 laser pulses (i.e., deposition time of 2500 s). X-ray analysis of the crystal indicated single phase within resolution. Rocking curves (ω-scans) were broad but identical for film and substrate within experimental resolution, indicating that the film is following the crystalline template of the substrate. θ-2θ scans through the film and substrate lines indicate a $2\theta_{substrate}$-$2\theta_{film}$ = 0.24° (see Fig. 2). With a*($KTaO_3$) = 3.989 Å, we calculated c†(film) = 4.009 Å. With a unit cell volume for $KTaO_3$ of $V(KTaO_3)$ = 63.47 Å^3 and for $KNbO_3$ of $V(KNbO_3)$ = 64.74 Å^3, as well as the assumption that $V(\text{film}) \leq [c(\text{film})]^3$ = 64.433 Å^3, we found that $x \leq 0.75$. This assumption is based on the fact that the in-plane film lattice parameter (grown on a substrate with a smaller lattice parameter) will not be larger than the out-

*In-plane lattice parameter.
†Normal lattice parameter.

of-plane value. However, the opposite extreme estimate is to propose that the in-plane lattice parameter of the film is identical to that of the substrate (which is an unlikely case for a film of this thickness). This would lead to V(film) = $a(KTaO_3)^2 \times c$(film) = 63.79 Å^2, leading to $x \geq 0.25$. From optical growth monitoring and previous experience, we assume that the growth rate for $KNbO_3$ is only slightly larger than that of $KTaO_3$ (this depends on target quality), and therefore that $x \approx 0.5$. Using T_c[°C] = 676°C · x –241°C, we find that –72°C ≤ T_c (film) ≤ 266°C from X-ray data, with the mean value being T_c = 97°C. Using data from Christen et al. [*Thin Solid Films* **312**, 156 (1998)], we know that $\partial\varepsilon/\partial T$ is highest for $T = T_c - 50$°C; therefore, the film appears to have the appropriate composition. (Extensive characterization via an outside sub-contract would have to be performed to determine this number accurately.) Optical microscopy revealed defects at the surface of the film on portions of the substrate ("milky" regions), with most of the substrate being coated with a nice-quality epitaxial smooth film.

After thin films of $KTa_{1-x}Nb_xO_3$ were successfully fabricated, both $KTa_{1-x}Nb_xO_3$ and $LiNbO_3$ SAW delay lines were designed assuming a foundry with a 2-µm technology. In the following summary of the design, $LiNbO_3$ has been used as the example; however, the design principles are the same in both cases.

The 2-µm line width constraint allows sufficiently thick aluminum (120 nm) to eliminate the need for secondary metallization on the bond pads while staying below the manufacturing constraint of a 10:1 width-to-thickness ratio. An objective was to minimize the size of the active area of the SAW temperature sensor. This dictated that the transducer period be minimized. The only remaining parameter that dictates the size of the active device area is the number of electrodes per transducer period. Two-electrode-per-period (2/λ) transducers exhibit serious distortions from internal reflections. Four electrode-per-wavelength (4/λ) transducers are preferred for delay lines since they are mechanically reflectionless. Three-electrode-per-wavelength (3/λ) transducers are also reflectionless and this was the style selected for the design. The transducer period was thus 12 µm with three lines and three spaces of 2 µm per electrode (i.e., with equal electrode spacing, each line or space is 2 µm).

The transducer bandwidth is the center frequency, F_c, divided by the effective number of transducer periods, N. Thus, any bandwidth specification would determine the number of periods. In practice, bandwidth specification is of less practical importance for the application under consideration. Therefore, the number of electrode periods was iteratively adjusted to optimize insertion loss and other electrical properties. A 12-period transducer was found to be optimal. The center-to-center transducer separation (L_{cc}) in wavelengths determines the slope of the phase shift at center frequency and, along with the number of transducer periods, N, the number of 2π phase shifts in the transducer pass band. A value of L_{cc} = 112 was chosen to balance device size with phase resolution. Thus the total active device width in microns was

$$(12 \times 12 \times 2 + 112 \times 12) = 1632\ \mu\text{m, or } \sim 1.6\ \text{mm} \quad .$$

Using an aspect ratio (length to width) of 6:1 (typical in delay line design), the active device area was therefore ~0.27 mm × 1.6 mm.

The nominal phase shift is given by

$$\textit{Nominal Phase Shift} = 360° * L_{CC} = 40{,}320° \quad . \qquad (4)$$

Thus, a 0.1° phase resolution would correspond to ~2.5 parts per million (ppm) of the nominal phase shift. With a temperature coefficient of phase of 75 ppm/K, the sensor should have a nominal temperature resolution of 0.033 K (33 mK).

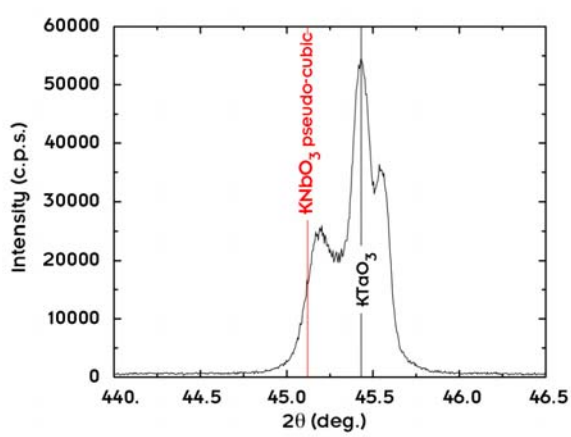

Fig. 2. Film and substrate X-ray diffraction (θ-2θ) peaks for the $KTa_{1-x}Nb_xO_3$ film on the $KTaO_3$ substrate.

Results and Accomplishments

The phase response as a function of temperature for KTN as well as $LiNbO_3$ were measured with a network analyzer by heating the device in one-degree increments and measuring the phase at each temperature. The response is shown in Fig. 3. The slope of the phase (i.e., the change in phase per degree change in temperature) as a function of temperature is shown in Fig. 4. Comparison of KTN and $LiNbO_3$ responses from these two figures show the following:

1. The largest phase change exhibited by the $LiNbO_3$ is about –4.7°/°C, whereas the largest phase change exhibited by the KTN is about twice as much (11°/°C). Assuming that the network analyzer phase resolution is at least 0.5°, this corresponds to a temperature resolution of 0.1°C for the $LiNbO_3$ and better than 0.05°C for the KTN.

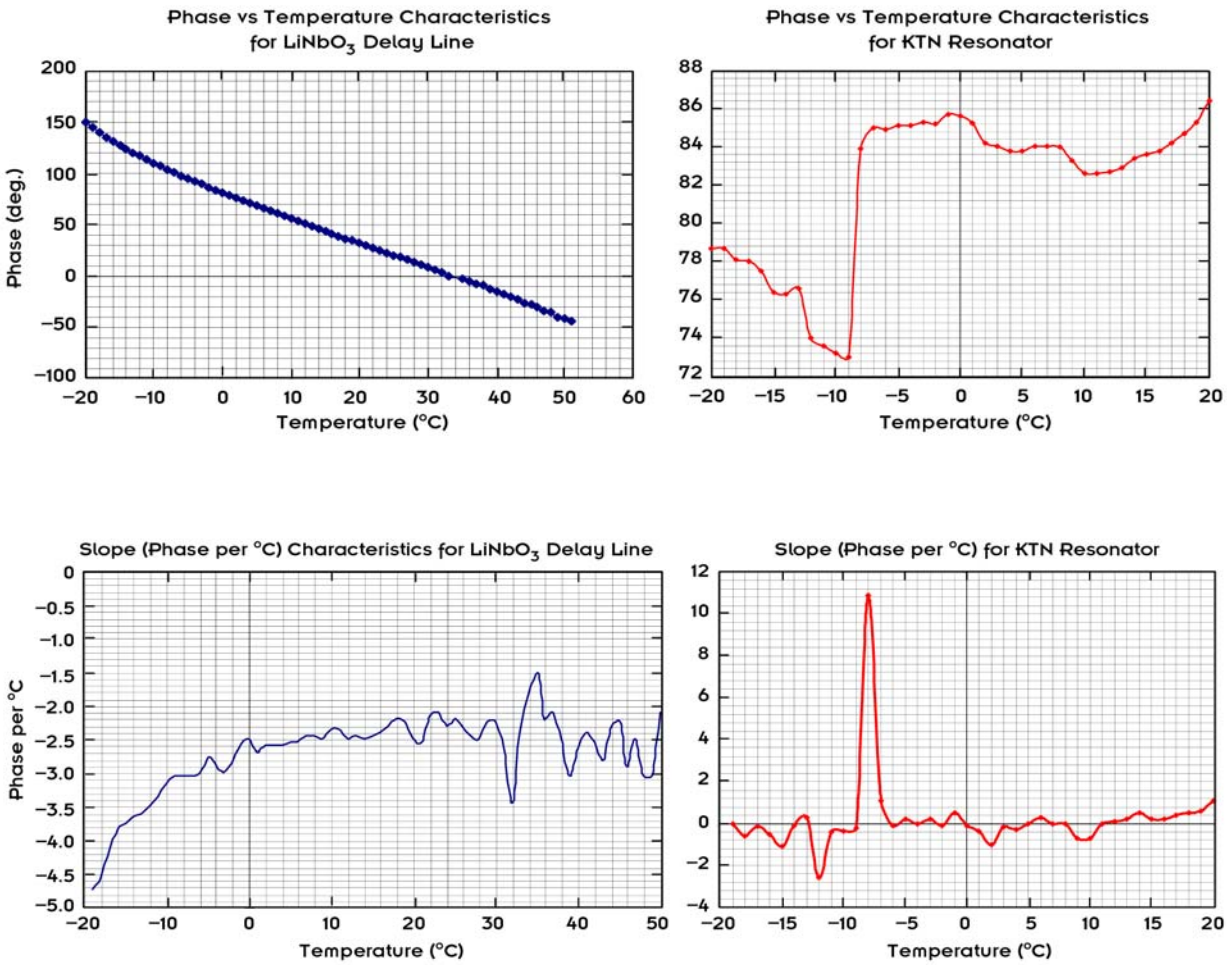

Fig. 4. Slope of phase as a function of temperature for $LiNbO_3$ and KTN SAW structures.

2. The temperature response of KTN does exhibit the characteristics the investigators were hoping for. However, the investigators believe that optimum response was not achieved due to fabrication difficulties (e.g., poor photolithography by the company that fabricated the SAW devices, learning curve in fabricating KTN SAW structures, etc.).

Summary and Conclusions

This study was successful in identifying KTN as a potential candidate for IR detection and imaging. With improved fabrication and signal processing, it will be possible to achieve a temperature resolution of better than 0.05°C. One observation that needs further study is that theoretical predictions placed the transition temperature within a wide temperature range (between –72°C and 266°C), the arithmetic mean of which gives a value of 97°C. We therefore expected the maximum phase changes to occur at a higher temperature than what the results indicate (–8°C). This apparent discrepancy will be a subject of subsequent studies.

Typical pixel size of current IR cameras is in the neighborhood of 50 µm. The "pixel" size of the sensor designed for this study was considerably larger. However, size was not a constraint for this initial study. We have identified a path for reducing the pixel size and using a different signal processing approach (to increase data acquisition speed in an array configuration) in subsequent studies.

References

[1]H. Mathews, *Surface Acoustic Wave Filters: Design, Construction, and Use*, John Wiley and Sons, New York, 1977.

[2]D. S. Ballantine et al., *Acoustic Wave Sensors: Theory, Design, and Physico-Chemical Applications*, Academic Press, 1997.

[3]H.-M. Christen, D. P. Norton, L. A. Gea, and L. A. Boatner, "Pulsed Laser Deposition of Soli-Solution Films Using Segmented Targets," *Thin Solid Films* **312**, 156–159 (1998).

High-Resolution, Real-Time, Three-Dimensional Imaging Using Two-Wavelength Spatially Heterodyned Interferometry

G. R. Hanson, P. R. Bingham, T. P. Karnowski, and J. T. Simpson
Engineering Science and Technology Division

The ability to make high-resolution, three-dimensional surface topology measurements in real time for inspection and metrology is a growing need in manufacturing, scientific research, stockpile stewardship, and medicine. The problem with existing topography methods is that they suffer from low-resolution, slow inspection speeds, and/or the inability to image large height changes with high spatial resolution. ORNL researchers have previously developed the Direct-to-Digital Holography (DDH) technique for imaging semiconductor wafers during the manufacturing process. DDH records the complete surface profile in a single digital image by using "spatial-heterodyning" to record the phase of the laser beam reflected off of the surface. This technique is ideal for surface topography measurements on wafers because the transverse (x, y) resolution requirements are of order 100–300 nm (of order 1/2 the laser wavelength), and the longitudinal (z) resolution requirements are of order 1–5 nm (much less than the laser wavelength). However, many potential applications involve longitudinal and transverse dimensions that are 10 to 1000 times greater than the probing laser wavelength. We have demonstrated a novel method of using two separate laser wavelengths to image the object surface. This method will allow high-speed or real-time inspection of surfaces with topological features in the 1- to 1000-μm range.

Introduction

The ORNL patented Direct to Digital Holography (DDH) technology uses holographic techniques along with digital image processing to measure and display surface profiles in real-time (more than 30 images per second is possible). The technology has been licensed to a start-up company and is currently being used in the development of a tool to image semiconductor wafers during the manufacturing process.

DDH has had limited impact on other industrial applications due to a significant limitation: surface profile features (both surface roughness and discontinuities) that exceed half of the laser wavelength are difficult to measure due to "phase wrapping." Skateboarders, figure skaters, and other extreme sport enthusiasts are familiar with phase wrapping, although they do not refer to it as such. Essentially, a 360-degree turn is equivalent to a 720-degree turn or even a 3600-degree turn in terms of the starting and finishing position.

In DDH, we are measuring the phase of a reflected laser beam whose wavefront encodes the surface depths. The surfaces must be relatively flat and smooth relative to the laser wavelength, with only a limited distribution of three-dimensional surface features. When the surface-feature depths and/or surface roughness exceeds half the wavelength of the measurement laser over a distance less than 2 pixels in the digital image, we find that the true depth becomes impossible to measure exactly (the reflective nature of our system imposes the half-wavelength criteria). Because the phase "wraps around," that is, goes through a 360-degree or 2π radian change, we cannot measure depths greater than a half-wavelength accurately, since the number of potential wraps past 2π is unknown. We are able to get a high-resolution measurement to within a half-wavelength, but we cannot measure multiple wavelengths with certainty.

The problem of phase unwrapping has been addressed in literature;[1,2] most techniques rely on a priori knowledge of the general characteristics of the surface under measurement and attempt to track phase wraps in an incremental fashion. However, these techniques require that the phase wraps occur over a large number of image pixels; a gradual slope can be tracked, but a sudden jump or too sharp a slope cannot be unwrapped (see Fig. 1).

To eliminate this problem, it would be desirable to measure the height variations at a much longer wavelength while still maintaining the longitudinal resolution of the shorter laser wavelength. This goal is accomplished in other forms of interferometry by acquiring the phase data at two or more wavelengths using multiple images and then looking at the difference of the phases measured by each wavelength.

We propose a new method for performing two-wavelength differential-phase interferometric imaging in a single digital image. This is not possible with existing types of digital holography or interferometry systems.

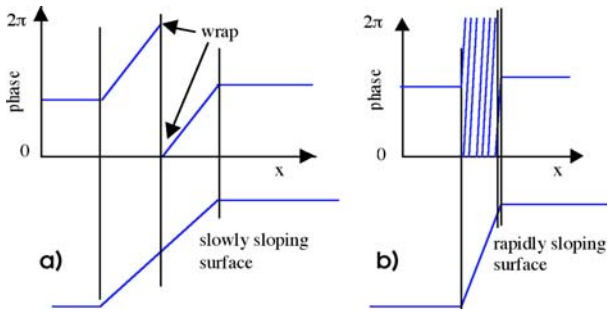

Fig. 1. In the gently sloping surface of (a), the phase can be unwrapped easily; in the steep sloping surface of (b), the problem is more difficult. Surface roughness can increase the difficulties in phase unwrapping tremendously. In addition, the limited number of pixels in an imaging sensor can also prevent unwrapping.

The technique of using two wavelengths to measure large objects is well known in digital holography, holographic contouring, and holographic interferometry.[3] In these techniques, phase information is obtained independently at two separate wavelengths. These two sets of phase data are then subtracted to transform the phase data to a scale length equal to the beat wavelength λ_b, where $\lambda_b = \lambda_1 * \lambda_2/(\lambda_1 - \lambda_2)$. Thus the phase is measured at an effective wavelength much longer than either of the two probing wavelengths. In this way, height variations many times greater than the original laser wavelengths used can be measured. This approach to two-wavelength measurements can be performed using DDH by sequentially (separate digital images) recording phase images at two different wavelengths, and then obtaining their difference. However, this sequential technique suffers from several limitations. First, noise in each individual image will be uncorrelated. The phase-image noise results in height errors proportional to the laser wavelength. When the difference between the two images is taken, the noise will be carried into the difference-phase image, but now it will be proportional to the beat wavelength λ_b. Thus the image quality and accuracy will be severely degraded. Second, any motion in the object between the acquisition of each image will result in pixel-to-pixel differences between the images. When the two phase images are subtracted, new errors will be introduced due to the pixel-to-pixel changes. Finally, acquiring each phase image sequentially increases the imaging time and limits the real-time ability of a potential system.

If the two phase-images could be obtained simultaneously using the same optics and digital camera, high-resolution differential-phase images could be generated. Image noise will be reduced because common-mode noise, vibrations etc. will be correlated and cancel out when the difference image is obtained. Since the two phase-images are obtained simultaneously in the same optics system with one digital camera, there is always exact pixel-to-pixel alignment and correlation. Finally, real-time topography is still achievable because only one image is required at each inspection location.

Technical Approach

This project will first demonstrate the ability to perform spatial-heterodyne interferometric imaging utilizing two laser wavelengths. By recording the two individual spatial-heterodyne interferograms and then taking the difference of the two phase images, object heights much greater than either individual wavelength can be measured. After demonstrating this novel technique, we will explore its capabilities and limitations.

Results and Accomplishments

We have successfully demonstrated the ability to record two spatial-heterodyne interferograms at different laser wavelengths. The recording of both wavelengths permits the imaging and inspection of objects with height variations much greater than either individual wavelength in real time. Utilizing two different laser wavelengths, we have accurately measured step height changes from a few hundred nanometers to over 6 µm. Figure 2 shows an example of a measurement made with the two-wavelength system on a sample with areas 2.86 µm high. The two individual wavelengths (left and center images) were unable to measure this height properly due to the many wraps; however, by beating the two wavelengths together, the third image shows proper measurement of the height. We have also imaged curved surfaces having tens-of-micrometers-of-height change over the image area. An example of this is the images of a convex mirror with a 52.8-mm radius of curvature shown in Fig. 3. The left and center images show the phase information obtained by the two individual wavelengths, while the right shows the beat wavelength image. This example quickly demonstrates the advantage of the beat wavelength. For this mirror surface, only one wrap appears in the beat wavelength image, while over 30 wraps occur in the individual wavelength images. The shape of the mirror

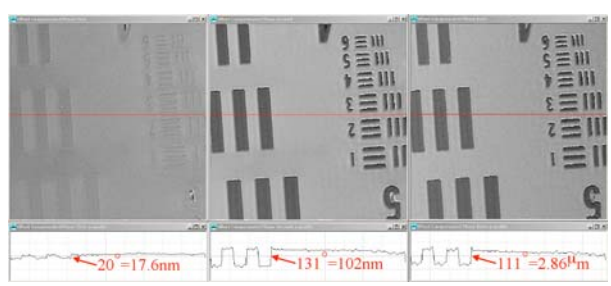

Fig. 2. Two-wavelength DDH imagery of 2.8-µm-deep resolution target. Left: 632.8-nm wavelength phase image; center: 611.9-nm wavelength phase image; right: 18.5-µm beat wavelength image.

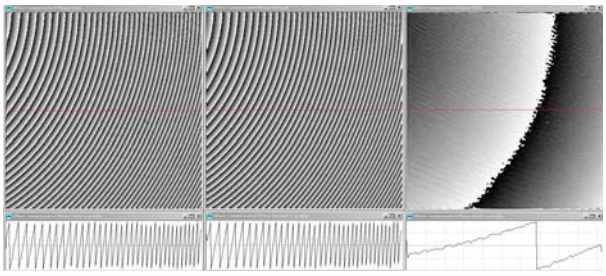

Fig. 3. Two-wavelength DDH imagery of concave mirror with 52.8-mm radius of curvature. Left: 632.8-nm wavelength phase image; center: 611.9-nm wavelength phase image; right: 18.5-µm beat wavelength image.

surface could be determined by unwrapping the individual wavelength images; however, phase unwrapping is a complicated problem that is greatly affected by noise in the image. A key limitation we have discovered is that the object surface roughness must be less than half the laser wavelength to successfully obtain a spatial-heterodyne interferogram. This limitation may reduce the range of potential applications.

We have utilized our experimental system to support the Spallation Neutron Source (SNS) Target Development program. The stainless steel vessel containing the mercury target material is damaged by cavitation in the mercury. Other inspection techniques available to the target group could not clearly resolve the depth of the pits caused by the cavitation. We used our system to measure the depth of these pits, which were from 10 to 50 µm across and from 1 to 10 µ/µm deep.

Summary and Conclusions

The successful demonstration of this technology has led to a joint proposal submitted to the National Institute of Standards and Technology—Advanced Technology Program (NIST-ATP) entitled "Spatial-Heterodyne Differential Digital Interferometry for MEMS Inspection." We are partnering with MicroSystem Technologies, Inc., to submit this proposal. Announcement of winners is expected by June 2003.

This project has also allowed us to build up a flexible laboratory capability to perform the spatial-heterodyne imaging. This has allowed us to begin a project with International SEMATECH to demonstrate some novel inspection capabilities of interest to the semiconductor industry.

References

[1]J. Strand and T. Taxt, "Performance Evaluation of Two-Dimensional Phase Unwrapping Algorithms," *Applied Optics* **38**(20), 4333–4344 (July 1999).

[2]D. Bone, "Fourier Fringe Analysis: The Two-Dimensional Phase Unwrapping Problem," *Applied Optics* **30**(25), 3627–3632 (September 1991).

[3]Wagner et al., "Direct shape measurement by digital wavefront reconstruction and multi-wavelength contouring," *Opt. Eng.* **39**(1), 79–85 (January 2000).

Signal Processing Architectures for Maskless Lithography

T. P. Karnowski,[1] D. Joy,[2] L. F. Allard,[2] and L. Clonts[1]
[1]*Engineering Science and Technology Division*
[2]*Metals and Ceramics Division*

In this work we analyze a redundant scanning array (RSA) geometry for low-energy, electron-beam maskless lithography. We then show estimates of the relationship between emitter spacing, gray levels, redundancy, and the printing accuracy as simulated by an image processing–based simple resist exposure and development model. We propose data compression architecture and algorithms to efficiently transfer control and printing data to the emitter array. Finally we present some experimental results determined with simulation software.

Introduction

Moore's law (i.e., the number of transistors on a microchip will double every 18 months) has become a driver for the semiconductor industry. Lithographic processes for printing device structures on integrated circuits (ICs) are the fundamental technology that has allowed this trend to persist. As device features shrink towards 130 nm, next-generation technologies for lithography are under frenzied development to replace optical lithography by the 100-nm technology node in 2005 and achieve 35-nm structures by 2014.[1] Electron-beam direct-write (EBDW) technologies provide the highest potential for maskless lithography (ML2). The International Technology Roadmap for Semiconductors (ITRS) states that "breakthroughs in direct-write technologies that achieve high throughput would be a significant paradigm shift [that] would eliminate the need for masks, offering inherent cost and cycle-time reductions."

ML2 methods such as EBDW have a unique advantage over the competing technologies: the long, tedious, and expensive process of fabricating a unique mask for the manufactured chip is not necessary. The costs of fabricating, inspecting, maintaining, and cataloging masks for alternate lithographic processes, along with the potential for yield loss associated with mask errors, are significant forces driving towards a maskless technology. While the increased mask cost can be amortized over the life of a particular IC product, such as a memory or microprocessor device, the ability to recover these costs in an application-specific integrated circuit (ASIC) foundry is highly problematic. In this case, a foundry rarely produces large quantities of devices for any given customer and the mask cost will be difficult to recover for sub-100-nm features.

As the ITRS states, the semiconductor community is extremely excited about the possibility for ML2. However, there are some rather daunting problems with establishing ML2 as a viable commercial technology. The data rate necessary for ML2 to be competitive in manufacturing is estimated to be in the 1- to 10-terabit/s range[2], which is not feasible in the near future. There is also doubt that the competing technologies for the writing mechanisms and corresponding photoresist (or analogous medium) will be able to accurately produce the desired patterns necessary to produce multilayer semiconductor devices.[3] Despite these issues, the payoff of a ML2 system is so great that there are still many ongoing efforts in developing technology for this exciting field. Thus, ML2 has three critical elements that must be addressed if a commercially competitive technology is to evolve: (1) the development of a robust array of signal emitters or alternate maskless lithographic device (MLD); (2) a resist medium that is responsive to the signal radiation of (1); and (3) a signal processing strategy and architecture that will enable competitive throughputs. All of the known institutions that are addressing this problem today are focusing primarily on one of these three aspects of maskless lithography. ORNL has been addressing part (1) through the development of an EBDW system composed of vertically aligned array of carbon nanofibers (VACNFs) under the auspices of a Defense Advanced Research Projects Agency (DARPA) funded program in Advanced Lithography. Other researchers investigating issues of device throughput are concerned largely with data compression.[2] These efforts explore the throughput as an image compression problem and do not explore issues of maskless printing accuracy, different maskless devices, or on-chip electronic processing. The crux of the issue is that the compression technique can depend not only on the mask pattern itself

but also on the scanning technique and writer/resist physics—an approach that the current EBDW data path estimates have failed to consider. Our specific goal with this effort is to develop compression techniques for candidate ML2 systems that include both algorithms and hardware implementations. If successful, we envisioned that this project and our complementary VACNF effort could potentially establish ORNL as a leader in maskless lithography.

Technical Approach

Our technical approach consisted of three main tasks.

Model Maskless Lithography Printing

We first modeled the maskless lithography printing process through two subtasks: analysis of the redundant scanning array (RSA) geometry as described in ref. 4 and modeling the impulse response of low-energy electron beams in resist material. These subtasks are designed to produce accurate models for simulations to help assess printing quality under a variety of different array geometries, which is directly related to the quantity of data needed to produce lithographic patterns.

Determine Required Control Signals through Simulation

We next investigated techniques for accurately determining what control signals were required. These methods were needed because the true data rates must be determined, as well as the actual data needed to print the patterns, before an effective compression scheme could be adopted or developed. Our approach first applied algorithms and methods for determining the best discrete "weights" for a particular array geometry and lithographic pattern, then assigning these weights to the redundant discrete emitters to optimize potential compression.

Design and Conceptualize Algorithms and Hardware for High Throughput

Finally, using results of the previous tasks, we sought to find compression techniques and hardware implementations that would exploit the array and data properties to produce high throughput solutions. This task was admittedly somewhat speculative and possibly the most risky endeavor of the project.

Results and Accomplishments

Model Maskless Lithography Printing

We first explored the geometry issues associated with a tilted RSA. The RSA is a practical technique for using massively parallel arrays of binary energy emitters to perform lithography. An array is passed over the resist medium at an angle so that the discrete emitters fall coincident to one another. Combined with clocked writings, a much finer pitch can be achieved than the actual array spacing. In addition, the use of an RSA can alleviate problems associated with nonuniform emitters and discrete firing locations. The basic concept is illustrated in Fig. 1. From our analysis, we determined that the desired tilt angle is given by

$$tan(\Theta) = -k\frac{M}{N} \quad ,$$

where k is the ratio of the x and y emitter spacing (generally unity) and M and N are positive-only integer values that represent the row and column difference between coincident elements. Consequently, there are only discrete angles that satisfy the co-incidence requirements.

A more significant result of the RSA analysis was the expected number of steps (i.e., discrete emissions) required per second S:

$$S = \frac{R\left(\frac{d_y}{d_r}\right)^2}{T} \quad ,$$

where R = redundancy (i.e., the number of times that an emitter passes over a specific site on the wafer), T is the writing time (60 seconds), d_y the spacing between emitters,

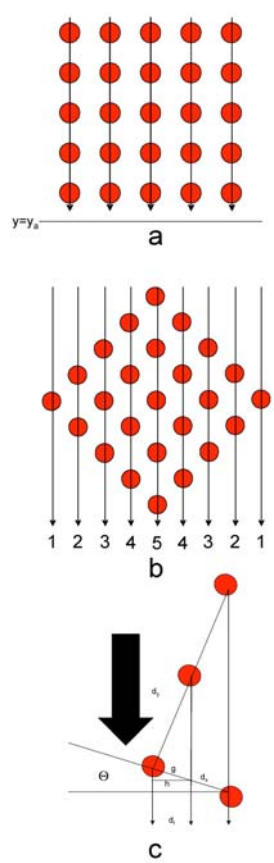

Fig. 1. The RSA concept. (a) An array with redundancy of 5. (b) Smaller array spacing produced with a tilted array. (c) Geometries and variables used to analyze the RSA.

and d_r the desired emission site spacing. We see that S is proportional to the square of the ratio of the actual spacing to the desired spacing. This makes sense since we are trying to create a fine discrete grid with more coarse elements in two dimensions, but such a result was not immediately obvious from the cleverness of the tilted array.

Our second subtask was the lithography system impulse response. We took the results of electron-beam profile experiments performed by David Joy and Larry Allard to create an approximate "system impulse response." The experiments were performed with Monte-Carlo simulations in PMMA, a resist material chosen for its general qualities. The results were not terribly encouraging, as the low energy used by candidate ML2 devices requires extremely thin layers of PMMA. There is considerable evidence that using a different type of resist—particularly chemically amplified resists—would be much more effective. We were not able to obtain material characteristics for any of these other candidates that would have allowed us to perform additional Monte Carlo experiments. A plot of this data is shown in Fig. 2. Nevertheless, this data was useful in creating a basic function and in examining how we may use it in performing maskless lithography. We were able to explore how scaling would be done on the function in association with different emitter spacings and redundancy factors or gray levels. We used an exponential curve fit to the data to determine a response modeled by

$$h(r) = \begin{cases} 1.8\frac{G}{R}, r \le 1 \\ \frac{G}{R} exp\left(-0.0283r^2 + 0.0613r - 1.0546\right) elsewhere \end{cases},$$

where G is the single-dose gain, R is the redundancy, and r is the distance from the center of the emitter. We show this response in Fig. 3.

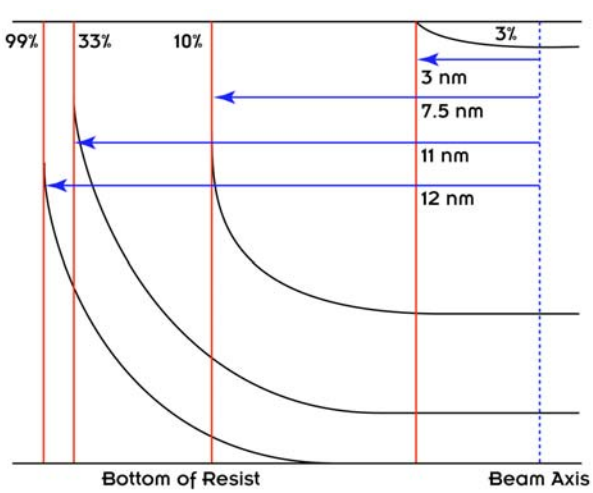

Fig. 2. The Monte Carlo simulations of the resist response.

Determine Required Control Signals through Simulation

The RSA geometry produces a number of discrete, approximately regularly spaced emission sites. We can model the printing process by weighting these sites with the number of "ON" emissions at each site, and convolving with the impulse response. Finally a threshold is applied to simulate the development process to produce a binary image that should match the desired pattern as closely as possible. These steps are illustrated in Fig. 4.

We used several different methods to try and determine optimal printing weights and examined the error produced by these methods. A few of our methods did not bear fruit, although they could stand to be revisited in the future. The most effective method was also the most time-consuming: an algorithm we call Direct Quantized Search (DQS) modeled after the direct binary search methods of ref. 5. We found that all our approaches produced errors, but of course more gray levels decreased errors. Determining what levels are appropriate is dependent on many factors, but we believe 16 gray levels seemed to work rather effectively with an effective (tilted RSA) spacing of 10 pixels, or 4 gray levels with a spacing of 5 pixels. Some examples of printed patterns with different spacings and redundancies are shown in Fig. 5. We were also able to use our simulation software to determine errors due to random emitter displacements and random emitter failures. The latter are shown in Fig. 6.

Design and Conceptualize Algorithms and Hardware for High Throughput

These results suggested a compression technique we called programmable basis functions (PBFs), which are geared toward very simple circuits that are located at each emitter and decode primitive code words for good compression rates. A block diagram of the circuitry for a decoder is shown in Fig. 7. When coupled with Huffman coding, they seem to be effective at reducing the data rate, but the rates we produced are still rather high because

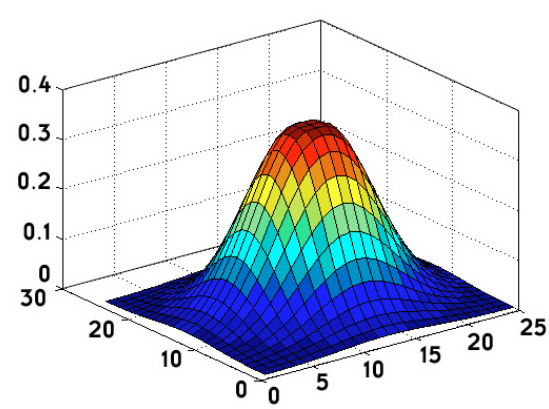

Fig. 3. 2-D plot of the modeled impulse response.

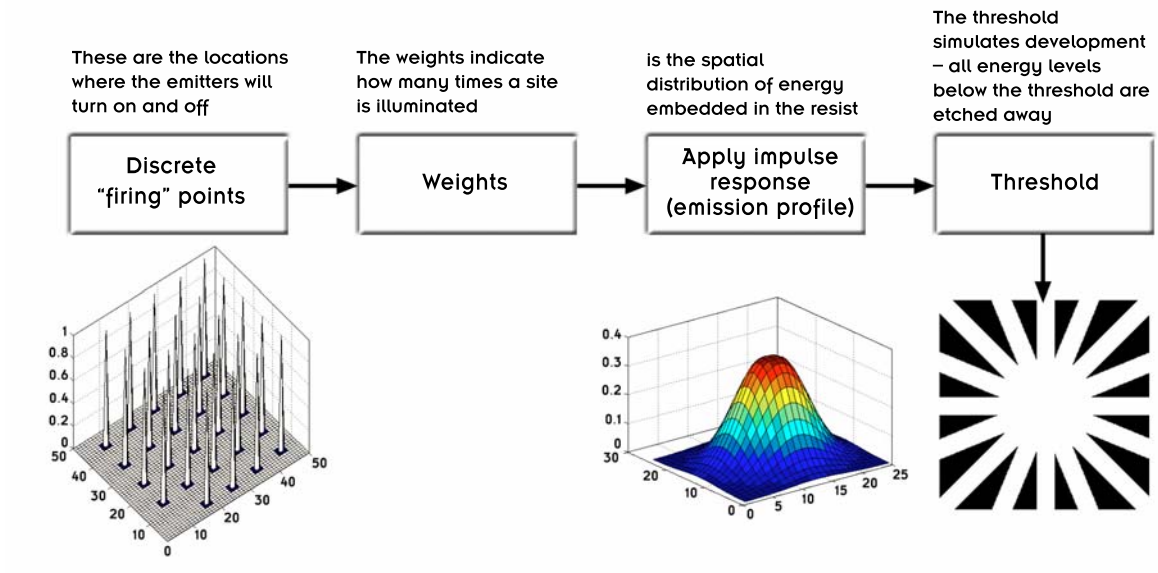

Fig. 4. System diagram of ML2 printing process simulations.

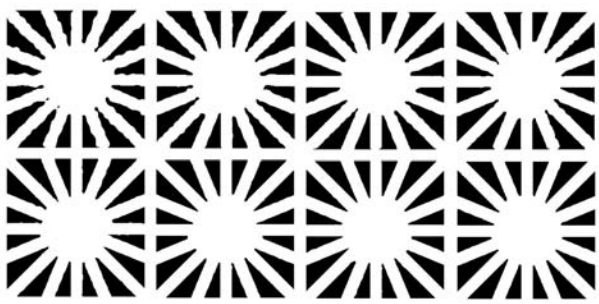

Fig. 5. Results with cross pattern and spacing of 10 (top) and 5 (bottom). R = 3,7,15,31.

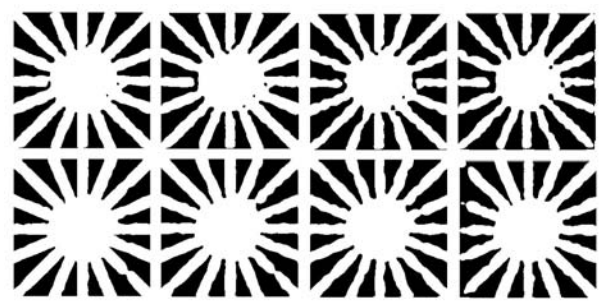

Fig. 6. Cross test images showing effects of random dead elements for 10%, 20%, 30%, and 40% bad elements. Top row: spacing = 10 pixels, R = 15; bottom row: spacing = 5 pixels, R = 3.

each decoder must be addressed at different times. In addition, for simplicity, we actually expand the data prior to transmission; for example, a redundancy of 15 can be represented as a 4-bit word, but because we seek simple circuitry, we actually issue 16 bits (prior to PBF and Huffman compression), which creates higher uncompressed data rates.

More encouraging, however, are the concepts of limited library compression (LLC) and a massively parallel optical data path. The LLC method was suggested by our printing simulation work. Researchers in this field have started with the concept that lossless compression is necessary, but the truth is that no ML2 device will produce a printed pattern that is exactly like the CAD files. The goal of LLC is to use a small library of control signals that produce a pattern that is "close enough" based on simulated print quality measurements. Similarly, we realized from our circuitry design and compression studies that an alternate data path would be beneficial. By using spatial light modulators or SLMs and using large arrays of photodetectors as the input devices, a more effective optical path could be created with relatively inexpensive components. This approach has some similarity to those used by some ML2 technologies, with the exception that our method transmits code words that can represent compressed data streams.

Summary and Conclusions

Our analysis revealed several problems we see with the creation of the ML2 system (besides creating the maskless writing device itself). These problems can be summarized as follows:

1. *The large data rates required*. Solutions seem to be compression methods (which take up a lot of chip real estate and require extremely large on-chip data rates as well) or a massively parallel optical solution (which requires either impossibly fast spatial light modulators, or photographic film storage mechanisms which may prove to be impractical).
2. *The ratio between the desired spacing and actual array spacing.* The tilted array is an ingenious idea,

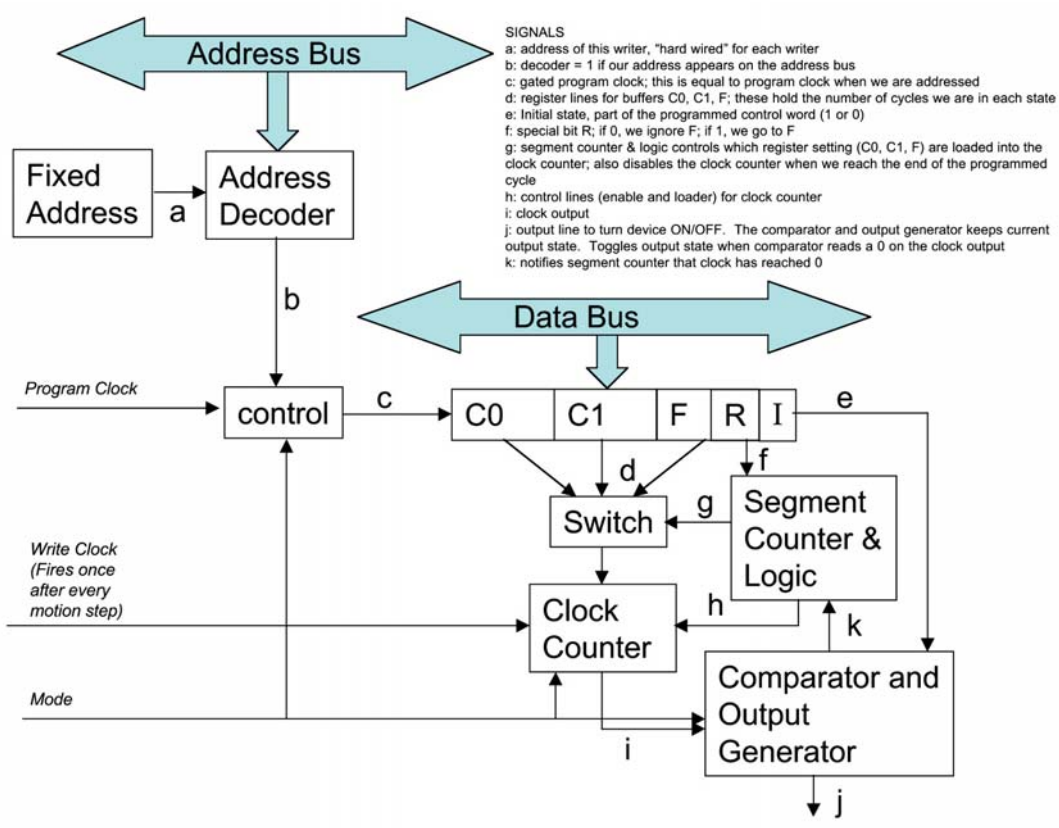

Fig. 7. Block diagram of PBF decoder circuit.

but it cannot get around the fact that many writing cycles are required to write a tight pattern with relatively sparsely spaced emitters. Due to the two-dimensional nature of the problem, the number of steps scales as the square of the ratio between the actual spacing and the desired spacing.

3. *The redundant scanning.* Again this is also an ingenious idea and very necessary to overcome the shortcomings of binary emitters, but the number of steps required scales linearly with the number of redundant elements desired.
4. *Creating the optimal weighting factors will be time-consuming.* This may be a fertile field for some clever solutions, however. The problem should be somewhat easy to scale, making it well suited for networked computer solutions.

We believe we have good solutions and directions for the following problems:

1. The LLC technique can help improve compression dramatically using very simple circuits for decoding.
2. Introducing signals through a massively parallel input stream, such as an optical path, would be an ideal way to input the data to the emitters.
3. Based on error measurements, we believe (if our simple thresholding is a reasonable practice) that lower gray levels than cited in ref. 2 can achieve effective results.
4. Missing elements can be a problem, as can motion problems, but these both are not show-stoppers if the impulse response of the system is considered in the weighting design.

Our next plans for this work involve three main efforts. We would like to determine if the LLC technique can succeed for larger circuits than our test patterns in these experiments. If that effort has merit, the compression technique could be useful for either an optical massively parallel method suggested here or even a more conventional electronic data path method. Finally, we explored some iterative techniques based on linear least-squares estimation and projections onto convex sets for the selection of the optimal weights. We believe these are important problems that could also bear fruitful research results.

This work has proceeded toward firmly establishing ORNL as a leader in maskless lithography systems engineering. We have submitted a white paper to selected government and nonprofit agencies (such as the Defense Advanced Research Projects Agency's Microelectronic Program), and we are optimistic that we will be able to

continue this research. In particular, our invention disclosures that are the direct result of this work represent radical new ideas for enabling technologies for maskless lithography which we believe will directly impact the future of this field.

References

[1]International Roadmap for Semiconductors, Semiconductor Industry Association, 1997.

[2]V. Dai and A. Zakhor "Lossless Layout Compression for Maskless Lithography Systems," *Proceedings of the SPIE: Emerging Lithography Techniques IV* **3997**, 467 (2000).

[3]D. Lammers, "EUV gains as venture ends e-beam litho work," EE Times, http://www.eetimes.com/story/OEG20010105S0023.

[4]L. R. Baylor, D. H. Lowndes, M. L. Simpson, C. E. Thomas, M. A. Guillorn, V. I. Merkulov, J. H. Whealton, E. D. Ellis, D. K. Hensley, and A. V. Melechko, "Digital electrostatic electron-beam array lithography," *J. Vacuum Science & Technology B* (Microelectronics and Nanometer Structures) **20,** 2646 (2002).

[5]J. P. Allebach, "DBS: retrospective and future directions [direct binary search]," p. 358 in *Proceedings of the SPIE, Color Imaging: Device-Independent Color, Color Hardcopy, and Graphic Arts VI*, Vol. 4300, 2001.

Fluorescence-Based Coatings Diagnostics

S. W. Allison and D. L. Beshears
Engineering Science and Technology Division

The protection of turbine blades and vanes by means of thermal barrier coatings (TBCs) is one of the key techniques that enable the envelope of turbine-engine operating temperature to be increased. Ensuring TBC integrity is vital for preventing hot section component failure. The role of the TBC is critical because failure of the TBC to be durable and to perform properly leads to severe engine damage. For example, if the TBC spalls off, it leads to temperature rise of the underlying substrate and exceeding of operational limits with possible subsequent failure. Ensuring TBC integrity is of concern to more than just the propulsion engine community, as evidenced by an assessment of the needs for sensors and controls for land-based advanced gas turbines that was performed for the Department of Energy.[1] This report indicated that, out of several critical instrumentation and sensor areas of concern, the requirement for a TBC failure and health monitoring capability was the number one need. We therefore conclude from this and other communications that a means for detecting TBC spallation on-line is of considerable value. The goal of this project was to develop approaches for long-term monitoring of TBC integrity via fluorescence techniques. The primary application is for operating turbine engines, but similar surfaces in other types of engines should also be viable.

Objective and Technical Approach

The objective of this project was to explore luminescence-based methods for diagnostics of TBC coatings. Layering of fluorescent materials can be the basis for heat-flux measurement, wear monitoring, temperature measurement, and overall coating health determination. Such a coating may consist of a thermal barrier coat, typically ytrria-stabilized zirconia (YSZ), and a thermographic phosphor on top and/or underneath the YSZ. As it turns out, YSZ can also be activated to fluoresce by doping with a rare earth so that it may function as a thermographic phosphor as well. The vision is to attain coatings whose layers are of controlled, known thickness and whose emissions are distinct. By monitoring the ratios of the characteristic emissions, the thickness and overall coating health may be determined. In principle, if the environment is clean, only two coatings may be required. In the event that soot or other material builds up on the coating, a third layer can provide added benefit by enabling the degree of attenuation of the soot coating to be inferred. By using an imaging system in conjunction with two or more fluorescent coatings, cracks may be more easily discernible. In such an application, incipient problems could be detected before catastrophic failure occurs.

The inset of Fig. 1 depicts three representative coatings for purposes of illustration. YSZ:Dy fluoresces in the yellow-orange and blue, YSZ:Tb fluoresces in the green and blue, and YSZ:Eu fluoresces mainly in the red. However, YSZ absorbs well in the near UV and blue so that appropriate visible wavelengths should be used for realistic thicknesses of the material. The physical properties of the coating are not expected to be significantly affected by the small doping level.

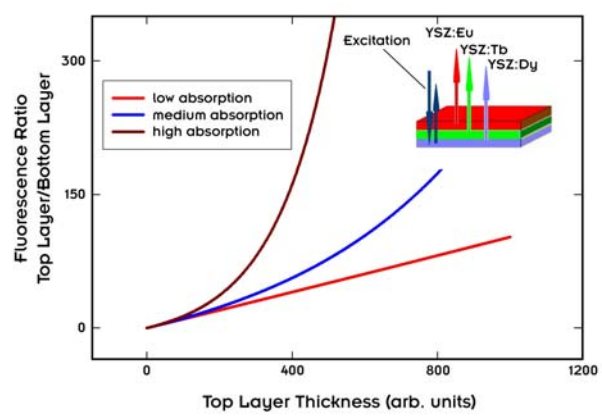

Fig. 1. Plot of fluorescence ratio versus top layer thickness.

A simple analysis provides instructive illustration of our approach. It begins with a derivation in ref. 2, which developed equations for emission from films of fluorescent dye mixtures. Consider a differential element of area in a film that is illuminated with excitation light. The fluorescence from such an element is

$$dI_f = I_e \cdot \alpha \cdot Q \cdot dx \quad , \tag{1}$$

where I_e is incident intensity, α is an effective absorption coefficient which includes scattering losses, Q is the quantum efficiency of the fluorescence, and dx is the film thickness. The well-known Lambert-Beer relation teaches that I_e will decrease as the excitation light penetrates the material according to

$$I_e(x) = I_0 e^{-\alpha x} \quad . \tag{2}$$

The differential fluorescing element becomes

$$dI_f = (I_0 e^{-\alpha x}) \cdot \alpha \cdot Q \cdot dx \quad . \tag{3}$$

The total fluorescence received by a detector for a single layer of thickness d is the integral of this expression times an appropriate collection efficiency, η

$$I_f = \eta \cdot \int_0^d \alpha \cdot Q \cdot I_0 \cdot e^{-\alpha x} dx = \eta \cdot I_0 Q \cdot (1 - e^{-\alpha d}) \tag{4}$$

$$I_f = \eta \cdot I_0 \cdot Q \cdot (1 - e^{-\alpha d}) \tag{5}$$

If we generalize and apply the above analysis successively to layers of two different materials of thicknesses d_1 and d_2, absorption coefficients of α_1 and α_2, for layers attached to a surface of reflectivity R, we may obtain the following two expressions for the received fluorescence at each fluorescence wavelength.

$$I_1 = I_0 \cdot \eta \cdot Q_1 \cdot \{(1 - e^{-\alpha_1 \cdot d_1}) + R \cdot (e^{-\alpha_1 \cdot d_1 - 2 \cdot \alpha_2 \cdot d_2}) \cdot (1 - e^{-\alpha_1 \cdot d_1})\} \tag{6}$$

$$I_2 = I_0 \cdot \eta \cdot Q_2 \cdot \{(e^{-\alpha_1 \cdot d_1}) \cdot (1 - e^{-\alpha_2 \cdot d_2}) + R \cdot (e^{-\alpha_1 \cdot d_1 - \alpha_2 \cdot d_2}) \cdot (1 - e^{-\alpha_2 \cdot d_2})\} \tag{7}$$

The ratio of I_1/I_2 is plotted in Fig. 1 as a function of the thickness, d_1, of the top layer. As expected, it is a well-defined function of the thickness of the top layer. If the absorption of the excitation light is low, then the dependence is approximately linear. Modeling reveals that the value of the substrate reflectivity does not change the position of the curves significantly. A more detailed model could be developed (for example, taking into account absorption of fluorescence in the layers which we now know can be significant for some of the shorter wavelengths), but what is presented here will suffice for the present purpose of illustrating our goal.

Results and Accomplishments

Given the above analysis, a number of steps are necessary to move forward toward demonstrating useful coatings diagnostics:

1. Determine the transmission of YSZ material.
2. Verify that top and bottom coatings can be viewed simultaneously throughout a useful temperature range.
3. Verify that rare-earth-doped YSZ material can fluoresce.
4. Place test coatings in operating degrading environments for in situ wear.
5. Obtain and test layered materials of known thicknesses.

In this project, we have collaborated with researchers at the NASA Glenn Research Center to address the first three steps, the results of which have been published.[3] Briefly, in regard to step 1, it was determined at NASA that YSZ is highly absorbing in the ultraviolet, near-ultraviolet, and into the blue region of the spectrum. This observation led to the use of visible excitation sources for further investigations. With respect to step 2, it was demonstrated both at ORNL and NASA that several phosphor materials coated underneath a YSZ could be excited from the top of the coating with green light at 532 nm. Emission could be distinguished spectrally as expected and also temporally. For example, YAG:Ce emission has a characteristically short decay time, around 60 ns, which is easily separable from typical longer-lived fluorescence that is many microseconds in duration. Measurements of top and bottom coatings were taken to 1100°C. With regard to step 3, several doped-YSZ materials were procured and emission spectra measured. This is represented in Fig. 2, which shows the characteristic emission spectra of two such materials, YSZ:Dy and YSZ:Eu. These materials exhibited the expected relatively narrow band emission that is desired. Future tests will characterize these materials versus temperature. For step 4, follow-on work is in progress regarding testing coatings in an operating environment. With regard to step 5, we did not obtained samples for detailed testing before the project completion date.

Overall, excellent progress in the development of fluorescent coatings techniques was made. During the course of work with NASA, an additional unexpected benefit appeared. Careful observation at NASA of a Y_2O_3:Eu coating measured the temperature dependence of the risetime of this material in this situation. We continued a study[4] of this emission feature and concluded that measurement of risetime promises to be another useful tool for thermometry and coatings health monitoring. The decay time of Y_2O_3:Eu is a sensitive function of temperature above about 600°C, as is well known, and it has been used effectively for thermometry above that value in the past. The risetime has the advantage that it is temperature dependent from at least ambient to well above 600°C. We have made a detailed study of the temperature dependence from a crystalline sample of Y_2O_3:Eu with the dopant at 0.5% and have compared it with the NASA data. The results are presented in Fig. 3. It is seen that our crystalline sample has a greater temperature dependence as well as longer overall risetimes. It appears that dopant concentration affects the risetime value and its temperature dependence. It is seen from the figure that temperature sensitivity is increased by decreasing the Eu concentration.

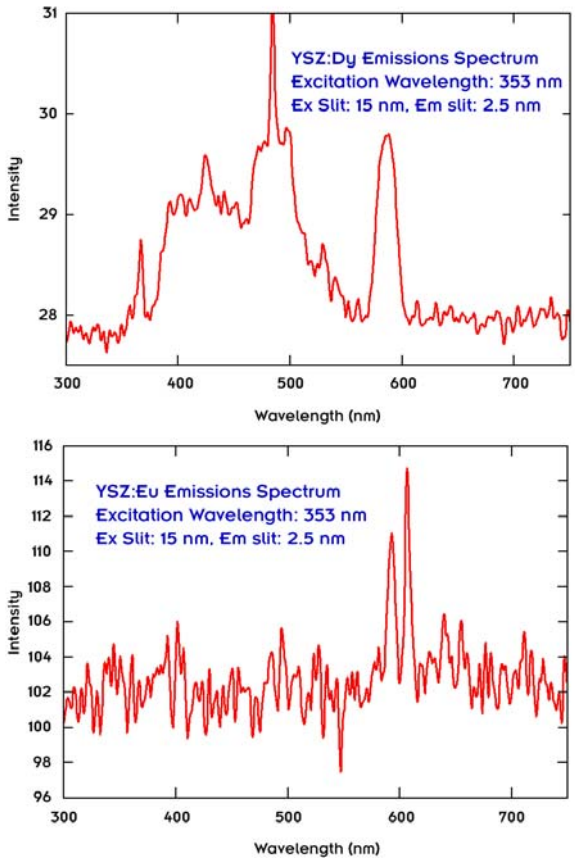

Fig. 2. Emission spectra of YSZ:Dy and YSZ:Eu.

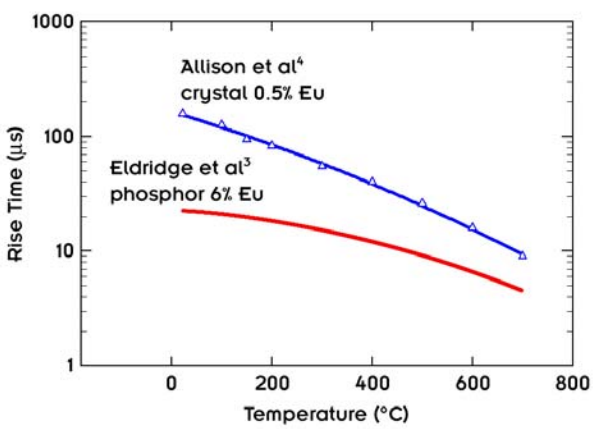

Fig. 3. Comparison of fluorescence risetime versus temperature for different Y_2O_3:Eu samples.

Summary

DOE, the Air Force, and NASA all have applications that can benefit from this research. In particular, we have participated with the Propulsion Instrumentation Working Group on a proposal for a specific Air Force program aimed at developing a thermal barrier coat health monitoring system for very-long-distance fighter jet turbine applications. The first such proposal was not successful, but we envision other opportunities. That proposal involved Rolls Royce, Pratt Whitney, Honeywell, Rolls Royce, and NASA Glenn. We are presently directing our effort at participating in a new joint US-UK Energy Partnership which DOE has promised to fund in FY 2005. A white paper has been submitted for turbine surface health monitoring.

References

[1]R. L. Anderson et al., *Advanced Turbine Systems Sensors and Controls Needs Assessment Study Final Report*, Oak Ridge National Laboratory report ORNL/TM-13335, February 1997.

[2]C. H. Hidrovo and D. P. Hart, "Emission reabsorption laser induced fluorescence (ERLIF) film thickness measurement," *Meas. Sci. Technol.* **12**, 467–477 (2001).

[3]J. I. Eldridge, T. J. Bencic, S. W. Allison, and D. L. Beshears, "Depth-Penetrating Temperature Measurements of Thermal Barrier Coatings Incorporating Thermographic Phosphors," accepted for publication in the *Journal of Thermal Spray Technology*.

[4]S. W. Allison, S. M. Goedeke, M. R. Cates, W. A. Hollerman, and T. J. Bencic, "Advances in High Temperature Fluorescence-Based Thermometry," CD-ROM, Huntsville, AL USA, Advanced Sensor Development Consortium Meeting, NASA MSFC, Huntsville, AL USA, 05/13/2003–05/15/2003.

Ultraviolet Electroluminescent Device Development

S. W. Allison[1], A. Akerman[1], and P. Rack[2]
[1]*Engineering Science and Technology Division*
[2]*Materials Science Department, the University of Tennessee.*

The development of solid-state light sources in the ultraviolet has been a long-term goal of defense and commercial organizations. Many millions of dollars have been directed at extending the III-V nitride blue lasers and light emitting diodes into the ultraviolet region. The present endeavor aimed at pursuing a different approach, that of electroluminescence (EL) of rare-earth doped materials. The advantages include inherent ruggedness, narrow spectral bandwidth, and the fact that such light sources may be made arbitrarily large in area. Sensing, illumination, and security applications are anticipated.

Introduction

The goal was to develop and demonstrate an ultraviolet-emitting, alternating current, thin-film electroluminescent (ACTFEL) device. The approach utilized gadolinium-based phosphor materials. These are known to produce emission lines in the ultraviolet as a result of transitions of the Gd^{3+}activator. The two most prominent transitions are at 312 and 275 nm. The purpose in building and testing ultraviolet emitting devices was to demonstrate the feasibility for a variety of applications. An additional motivation was to acquire valuable experience in designing and fabricating electroluminescent devices. Miniature UV sources have applications such as biological agent detection, communications, lighting, sensors, and security applications. The attributes of ruggedness and all solid-state construction are of obvious advantage to these and other applications.

Technical Approach

Two approaches were pursued in demonstrating ultraviolet electroluminescence. One aimed at learning how to properly sputter thin films of the relevant materials for subsequent ACTFEL devices. The other explored the powder electroluminescence approach. It should be noted that the most efficient means for producing electroluminescence is from thin films though powder EL, an inexpensive and easy means for producing light output. During the course of this project, a magnetron sputtering device was acquired by the University of Tennessee and its first use was for depositing thin films of the desired materials.

Results and Accomplishments

Materials Development and Characterization

The first step was to characterize the ultraviolet-induced emission from candidate phosphor materials. Three types of Gd-doped phosphors were ordered and received. They all photoluminesced with reasonable efficiency. Interestingly, the emission of the ZnF_2:Gd phosphor is shifted slightly, about 2 nm, to higher energy with respect to the Y_2O_3:Gd and YAG:Gd phosphors. This difference may be useful spectroscopically. A comparison of their emission spectra with respect to an SO_2 absorption spectrum shows a different response to the respective wavelengths and may indicate a useful approach to SO_2 detection. Tests with ultraviolet excitation revealed that that photoluminescence from the Y_2O_3:Gd and YAG:Gd phosphors were comparable and about ten times greater

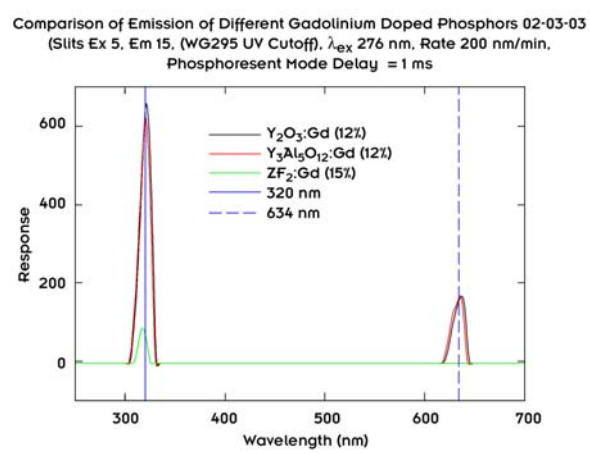

Fig. 1. Plot of ultraviolet photoluminescence of Y_2O_3:Gd, YAG:Gd, and ZnF_2:Gd.

than that for ZnF_2:Gd. This is depicted in Fig. 1. We recently acquired some thulium phosphors for other applications. It turns out that the Tm activator also exhibited useful, narrow-band near-UV light. Also, other standard visible electroluminescent phosphors, ZnS:Cu and ZnS:Mn, were characterized and exhibited their standard characteristics.

The next step in gaining experience and facility with electroluminescence was to construct a powder electroluminescence device. Commercially available night- lights are common examples of powder electroluminescence. Infrared, visible, and ultraviolet electroluminescence was achieved with some lab-made powder EL devices. Figure 2(a) is a photograph of one of a number of lamp assemblies that were made and tested for UV emission using many of the same potential UV candidate phosphors. A commercial night-light was cut and layer thicknesses measured. Following the layer structure and thickness measurements and literature accounts, electroluminescent structures were assembled using plastic, glass, or quartz windows coated with indium tin oxide (ITO) and tested using DC and AC excitation. Conditions were found under both types of excitation for electroluminescent operation in the visible using ZnS:Mn and ZnS:Cu. These glowed orange-yellow and blue-green, respectively, as expected and also exhibited a charging effect described in some literature accounts. Additional structures were built on the same lines, however, with the substitution of YAG:Tm, YAG:Gd, ZnF:Gd (various percentages and sources), Y_2O_3:Nd, and ZnS:Ag. Electrical excitation was provided in the same way as for the visible EL lamp structures, that is, using a high-voltage transformer.

The powder EL lamp consists of a phosphor layer sandwiched between two thin, clear-plastic insulators that in turn are sandwiched by brass screens. As an example, for ZnS:Mn, for transformer input at 450 Hz and 2000–4000 V, the center layer glowed orange-red through the brass screen; the higher the voltage, the brighter the light. With a stack thickness of 0.009 cm, the electric field was 2×10^5 V/cm to 4×10^5 V/cm. For YAG:Gd, using the same structure, but substituting phosphor layer, we observed UV emission at 312 nm as well as another UV wavelength, as was observed both with a monochromator and by secondary excitation of fluorescence from ZnS:Cu. Using the same structure, but substituting Y_2O_3:Nd, we observed IR with filters and a night vision scope, but not with the monochromator, possibly due to sensing choices. In fact this aspect of the project ended when serious mechanical problems with the monochromator developed. In addition to the brass screen, combinations of aluminum and partially transparent electronic ink–coated transparent insulators were used for electrodes with good results.

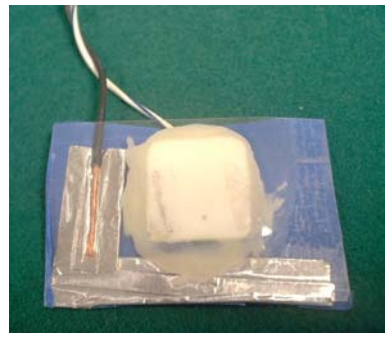

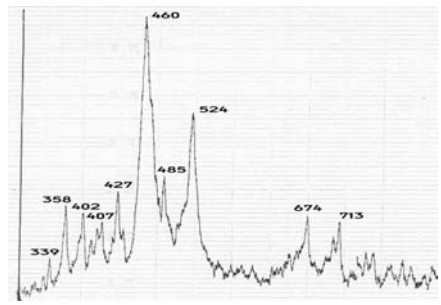

Fig. 2. (a) Photo of powder electroluminescence lamp and (b) emission spectrum of YAG:Tm powder luminescence lamp.

For some of the powder EL devices we detected some near ultraviolet emission that is characteristic of nitrogen. Other researchers see this in some instances also. This is not necessarily a disadvantage, just another source of ultraviolet light.

Representative results are presented in Fig. 2(b) for which a YAG:Tm powder EL lamp was tested using the monochromator scanning from 300 to 600 nm. The result was a spectrum similar to several seen in the literature with a peak near the expected emission, but with stronger peaks at 350 and 374 nm, also seen in the same papers. Using a Japanese ZnF:Gd formulation in a structure with pulsed excitation, a strong signal was observed with photomultiplier through a 313-nm narrow-band filter. Another filter centered at 360 nm allowed 1/5 the amount of signal under the same conditions. Turning the room lights on would "recharge" the lamp and allow a few minutes operation, typical of many of the visible structures fabricated. Subsequent attempts to measure the emission with a monochromator and photomultiplier were not successful due to the aforementioned mechanical problem.

Thin Film Electroluminescence

Gadolinium-doped thin films in yttrium oxide and yttrium aluminum garnet ($Y_3Al_5O_{12}$) were deposited on silicon substrates by radio-frequency magnetron sputtering.They exhibited the desired cathodo-luminescence (CL). This was typically on the order of

0.1%, depending on deposition parameters: substrate temperature, total chamber pressure, and the oxygen partial pressure. Post-process annealing also plays a role in final efficiency attained. Luminescence efficiency improved with increasing film crystallinity for films deposited at room temperature and subsequently annealed at 1000°C. Figure 3(a) shows a scanning electron microscope image of an Y_2O_3:Gd multilayer film, deposited on (001) Si, cleaved and shown in cross section. The film was deposited at room temperature and consists of five layers of Y_2O_3 and four layers of Gd. Figure 3(b) shows the emission spectrum for YAG:Gd and the emission intensity as a function of the dopant concentration. This curve peaks close to 6%. The corresponding figure for Y_2O_3:Gd is between 9 and 10%. These values are less than the maximal dopant concentrations of the neat phosphor powders. It is likely that this is due to thickness considerations. The details of the thin film development and characterization are provided in reports resulting from this effort.[1–4]

The one test of a thin film as part of an EL device on a substrate provided gratis by a commercial firm did not produce detectable luminescence. More testing would surely be successful.

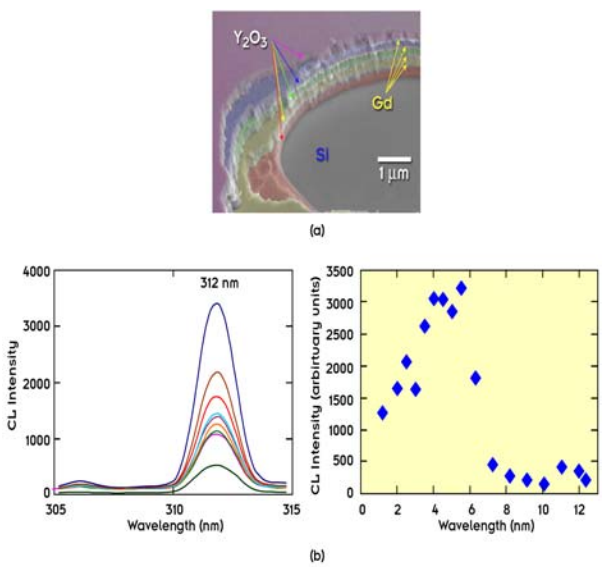

Fig. 3. (a) Y_2O_3 layer deposited by reactively sputtering yttrium in PO_2 = 0.212 mTorr and P_{Ar} = 2.788 mTorr with a forward yttrium gun power of 200 W. The Gd layer was deposited at 50 W in P_{Ar} = 3 mTorr and (b) cathodoluminescence intensity versus Gd concentration in the YAG films.

Summary and Benefits

Ultraviolet electroluminescence was demonstrated using the powder EL approach. Progress in sputtering and optimizing high-quality thin films for future use in thin film alternating current electroluminescent devices was made. The cathodoluminescence of the YAG and Y_2O_3 materials, doped with Gd, was significant. This may have positive implications for lighting since YAG materials are highly desired for white-light light-emitting diodes. We will further explore this application. Also, the powder luminescence approach may be pursued as a spectroscopic light source that is of simple construction and may be of use in high- temperature and hazardous environments as a robust spectroscopic ultraviolet light source. We will commence investigating opportunities within the Defense Advanced Research Projects Agency where this technology may be best suited.

References

[1]J. D. Fowlkes, P. D. Rack, R. Bansal, and J. M. Fitz-Gerald, "Cathodoluminescence Study of Gadolinium—Doped Yttrium Oxide Thin Films Deposited By Radio—Frequency Magnetron Sputtering," *Proceedings of the New Applications for Wide Bandgap Semiconductors Symposium of the Materials Research Society Spring Meeting*, **764**, C7.12 (2003).

[2]Y. Deng, J. D. Fowlkes, J. M. Fitz-Gerald, and P. D. Rack, "Combinatorial Thin Film Synthesis of Gd-doped $Y_3Al_5O_{12}$ Ultraviolet Emitting Materials," *Applied Physics D* (in press).

[3]J. D. Fowlkes and P. D. Rack, "Structure and Cathodoluminescence Relationships in Y_2O_3:Gd Thin Films Prepared by rf Magnetron Sputtering," *Applied Physics A* (manuscript in preparation).

[4]Y. Deng, J. D. Fowlkes, and P. D. Rack, "Structural and Cathodoluminescence Properties of $Y_3Al_5O_{12}$:Gd Films Prepared by a Combinatorial rf Magnetron Sputtering Technique," *Journal of Vacuum Science and Technology B* (manuscript in preparation).

Highly Reflective Subwavelength Structures for Homeland Security Initiatives

S. L. Jaiswal and S. R. McNeany
Engineering Science and Technology Division

In synchrony with many initiatives currently being undertaken in the interests of homeland security, the development of highly reflective subwavelength structures (SWSs) has application in areas of tracking, tagging, locating, and identification. These subwavelength structures are essentially customized optical surfaces, which become highly reflective when illuminated with light of a specific wavelength. Unlike other retro-reflectors, mirrors, and reflective paints, these subwavelength structures, if designed correctly, can offer high reflectance without limited wavelength selectivity, polarization selectivity, and angular sensitivity. The structures are essentially located in microscopic optical waveguides, with imprinted features, having dimensions smaller than the wavelength of the incident light. This offers an additional advantage over other highly reflective sources, which tend to be larger in extent and therefore difficult to conceal from visual inspection. This project investigated subwavelength optical structures with reflectivities in the infrared where long-range propagation (>5 km) of light in the atmosphere is possible. This is of particular interest due to the low absorption of infrared light with wavelengths in the range of 9–11 μm in the presence of fog, smoke, or dust. Thus applications of tags include remote identification, tracking, and locating at distances of 5 km or greater under a variety of environmental conditions.

Introduction

Examples of subwavelength optical structures, which provide customized reflectivities, occur in nature. One of the more publicized examples, discovered in the 1960s, is the moth eye effect. In this case, the moth's eye has been cleverly engineered to contain subwavelength-sized cones (cones with dimensions smaller than the visible light) that provide an antireflection coating[1,2] to conceal the presence of the moth. The SWS cones form a graded index layer in which Fresnel reflection losses are minimized at the surface. Previous work to customize surface reflectivities using physically etched structures has concentrated on coupling the incident light into an embedded waveguide via a surface relief grating. This configuration is termed a "guided mode resonance filter" and results in a multiple- layer structure that responds to a very narrow range of wavelengths.[3] In this proposal, a simpler configuration is employed, in which the surface relief grating acts as the waveguide itself. This structure is advantageous over existing technology since it offers high reflectance, without limited wavelength selectivity, polarization selectivity, and angular sensitivity, and can be employed for remote tracking (>5 km) with reasonable discretion.

Technical Approach

The use of periodic structures within a waveguide medium enables a form of optical control. In the commonest example, a diffraction grating systematically forces a spatial redistribution of uniformly illuminating light into a series of dark and bright regions, termed "diffraction orders." It is the design of the spatial frequency of the diffraction grating, relative to the frequency of the incident light, that determines the diffraction pattern. While diffraction patterns occur when the separation of ruled lines (or periodic structures) is just greater than the wavelength of incident light, it is interesting to explore the consequences of having the spatial separation smaller than the wavelength of the incident light. This is the subwavelength regime. By decreasing the separation, the resulting diffracted orders become more orthogonal to the incident light, until eventually a resonant condition is achieved at a specific separation where light coherently scatters from the interface between high and low refractive index, in such a way as to form a highly reflective beam and no transmitted orders. By depositing a thin film onto a lower refractive index substrate and patterning and etching the surface, periodic subwavelength relief structures are created that allow the surface itself to become an effective waveguide. These structures have a feature size of about 5 μm for the infrared regime under consideration (9–11 μm). Creating many of these structures on the order of magnitude of a "dust particle" and randomly orienting them can produce reflective beams from a wide range of incident angles, eliminating any angular selectivity concerns. In addition, these SWSs are consistent with the properties of photonic crystals, so that the feature size scales with wavelength, to produce high reflectance for any desired wavelength.

Design: The key factors to be considered are the waveguide materials and the design of the subwavelength structures in the wavelength of interest (9–11 μm in this case). Commercially available simulation software called Gsolver, based on rigorously coupled wave analysis, can easily model these structures.

Fabrication: The first goal is to create a thin-film waveguide. The likely candidate for the waveguide material is germanium, due to its high refractive index. Candidates for the substrate are $BaFl_2$, ZnSe, and ZnS with lower refractive indices, but this will be determined by the modeling results. The coating material will be evaporated onto the substrate using an electron-beam deposition tool. After determining the periodicity and feature size of the SWS, a photolithography mask will be designed and prepared. The SWS features are then patterned onto the surface using photolithography with sufficient resolution to perform the task. In order to etch the pattern into the waveguide, a reactive ion etcher will be employed. This will require the development of an etch recipe for the material of choice. Finally testing will be realized through a tunable (9–11 μm) CO_2 laser, centered at 10.6 μm, by illuminating the structure at normal incidence and using an appropriate infrared detector to measure reflectance.

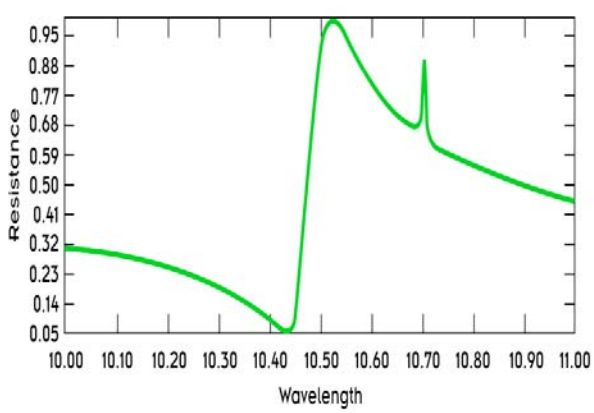

Fig. 1. Reflectance of a subwavelength structure in a germanium waveguide.

Results and Accomplishments

As noted above, the Gsolver computer program was used to model the optical performance of proposed subwavelength structures. Figure 1 gives an example of the calculated reflectance from SWS (an array of holes) in a 1-μm thin film of germanium on $BaFl_2$. Note the expected resonance peak in the reflectance curve near 10.6-μm wavelengths. Nearly total reflectance is expected at the resonance peak.

In an attempt to verify this type of optical behavior, efforts were undertaken to fabricate such structures at a micro-optics fabrication facility at Penn State University. Only one sample was produced that was tested for reflectance using a tunable CO_2 laser at ORNL. The sample was scanned over a wavelength range of approximately 9.5–11.5 μm. Unfortunately, the test results showed very little reflectance from the sample at any wavelength and no evidence of resonance structures.

Summary and Conclusions

Calculations of the optical performance of thin-film-based subwavelength structures clearly indicate that very high reflectance is possible. Unfortunately, the efforts to produce such structures as part of this project were unsuccessful. Nevertheless, because of the numerous potential applications and the high level of interest by potential sponsors for materials such as those investigated in this project, future research in technology will continue to be pursued.

References

[1]C. Bernhard, *Endeavor*, Vol. 26, p. 79, 196.

[2]P. B. Clapham, *Nature* **244** (5414), 281 (1973).

[3]R. R. Boye, "Physical Optics Approach to Guided Mode Resonance Filters," Ph.D. dissertation, University of Arizona, 2000.

A New Approach to Chemical Detection: Infrared Coherent Anti-Stokes Raman Scattering

R. K. Richards,[1] J. B. Wilgen,[1] M. R. Ally,[1] and M. Z. Martin[2]
[1]*Engineering Science and Technology Division*
[2]*Environmental Sciences Division*

We propose to revolutionize current thinking on making ultraperformance, small detectors for homeland defense, national security, and civilian uses by taking advantage of responses of chemicals in the relatively long wavelength electromagnetic (EM) spectrum for unambiguous identification of chemical threats. This is a completely unexplored area of investigation in sensor and detector development. This idea takes advantage of carbon dioxide (CO_2) lasers for a proof-of-principle demonstration. The technique is Coherent Anti-Stokes Raman Spectroscopy (CARS) using CO_2 lasers.

A proof-of-principle test was conducted using an innocuous chemical that has a nonlinear response in the microwave (long-wavelength) region. This idea has the potential to qualitatively change sensor and detector technology to exceed goals of the Pentagon, U.S. Department of State, and civil defense agencies for reliable, real-time information in case of chemical attacks or threats. We aim to provide early warning of a chemical warfare agent and eventually biological warfare agents released intentionally, for example, in a populated area to enable civil defense agencies to respond quickly. We should also be able to keep the first-generation unit cost under $10,000. We are motivated by our analysis to seek funding from DOE's Building Technology Program, Homeland Security Office, DoD, or DARPA to develop and demonstrate this potentially rewarding technology.

Introduction

Longer-wavelength CARS will have advantages over conventional CARS at shorter wavelengths, generally in the visible. The photon energy at 10-μm wavelength is only 0.1 eV (compared to 1.2 eV at 1 μm and 2.5 eV for visible CARS). Therefore, fewer resonances can be driven energetically by the lower-energy pump beam and the resulting spectra should be simpler. Appreciation of this idea is exemplified by considering the different responses of water molecules to visible and microwave energies. Heating water with visible light is inefficient even though visible light has higher energy per photon than microwaves. The reason why long-wavelength (such as microwave) heating of water is efficient (and convenient) is that water, like other chemical substances, has long-wavelength resonant frequencies, which respond well to this type of excitation. We intend to exploit the rotational and lower frequency modes of target compounds for positive identification. In addition, the frequency resolution provided by the heterodyne receiver will easily surpass even the highest-resolution visible spectrometers available today. Even simple molecules such as ammonia have extremely complicated infrared spectra. Simpler spectra with the ultimate in frequency resolution are the motivation for developing this technology to overcome a distinct limitation of existing instruments. Our goal is to build the next generation of high-performance, low-cost, extremely reliable, low-maintenance instruments for counterterrorism and homeland security.

Technical Approach

Ultrahigh-resolution CARS can be much more easily achievable at 10 μm than in the visible or near infrared. For CO_2 CARS, both pump beams would be produced by pulsed CO_2 lasers. The coherent output beam resulting from the CARS process would also be in the CO_2 wavelength range. A CO_2 heterodyne receiver would be used to down-convert the scattered signal to an intermediate frequency (IF) range of 1–30 GHz. By tuning the CO_2 local oscillator for the heterodyne receiver to make use of different lines in the 10 P series, a frequency range of 500 GHz, or more, can be covered. That allows access to >100 molecular lines from even a light molecule like methanol. Only this down-converted IF signal would be in the microwave/millimeter frequency range. Frequency resolution would then be determined by the resolution of the microwave/millimeter–wave spectrum analyzer, where frequencies can easily be measured to a fraction of a MHz. A significant part of the challenge is in achieving the necessary response time, as the frequency spectrum must be measured during a pulse time of <100 ns. At ORNL we have been using such heterodyne receivers for a fusion-

related diagnostic instrument and have developed leading-edge technology in pushing the frequency bandwidth and sensitivity of these CO_2 detectors/down converters for almost 20 years.

Our existing pulsed CO_2 lasers operate best at pulse power levels >10 MW, with pulse lengths of <100 ns, and are extremely reliable when operated in this low-power regime. At 10 μm the minimum spot size in the sample region will be 10 times bigger than it is for infrared CARS at 1μm. Except for a simple size scale-up by a factor of 10×, the scattering geometry would be the same as that developed for infrared CARS, consisting of two Gaussian beams intersecting at a small angle. Therefore, in order to achieve the same electric field in a cross-sectional area that is 100 times greater, the laser power must be 100 times greater (>10 MW versus >100 kW). That is possible, because it is difficult to degrade the power of pulsed CO_2 lasers below 10 MW. With the power level of the existing CO_2 lasers, instead of working hard to get the beam spot size down to a small dimension, we can comfortably accommodate sample volumes of less than 1 cc. Normally the CO_2 laser lines in the 10 P series (those around 10 μm) are spaced by about 53 GHz, so we could easily have the two pump frequencies separated by 53 GHz to probe for molecular resonances at that specific frequency. Continuous tuning of CO_2 lasers is done by raising the pressure in the laser cavity to 10 atmospheres, which can be accomplished in later developments of this diagnostic.

Results and Accomplishments

The core of the CO_2 CARS instrument consisted of five CO_2 lasers. Two high-power pulsed lasers were constructed as the source lasers, and these were driven by two seed lasers. The seed lasers set the wavelengths for the pulsed lasers. A fifth CO_2 laser was used as the local oscillator in the measurement of the resulting beam. The instrument is illustrated in Fig. 1 and shows the location of these lasers, the beam from the lasers, and the optical components. The detection of the resulting beam is with the heterodyne receiver, as illustrated in Fig.2. The beams from the two pulsed lasers were focused and directed to cross in a sample chamber containing a chemical to be studied. This chamber was constructed of one section of a laser cavity; it was 66 cm long and 10 cm in diameter. High-power laser windows (5-cm diam) were mounted to the ends of the sample chamber. With the two laser beams separated at the windows, the interaction length in the sample chamber was 50 cm. A photograph of the system showing the setup is provided in Fig. 3.

The first chemical selected for study was D_2O. This molecule was selected because it had a resonance at 54 GHz,[1] close to the primary frequency difference of the CO_2 lasers at 53 GHz and within the line width of several GHz. The chemical was added as a liquid in the bottom of the sample chamber (which was purged with dry air) and allowed to evaporate at room temperature, thus producing a partial vapor pressure of 17 Torr.

The two pulsed lasers were set to different laser wavelengths through the seed lasers. The higher-power

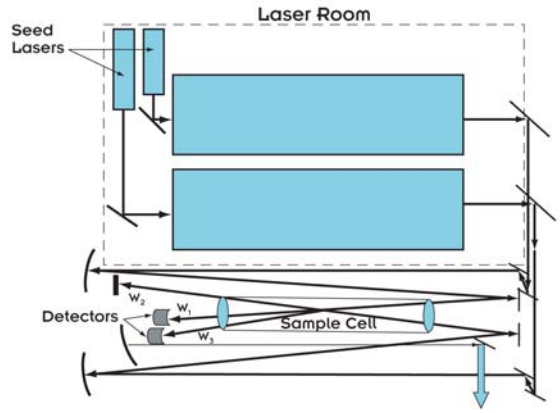

Fig. 1. Schematic of the CO_2 CARS instrument showing the location of the lasers, optical components, and sample chamber in the laser room.

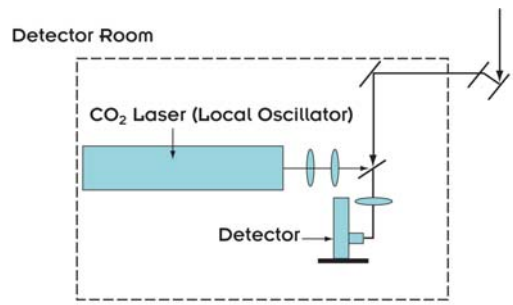

Fig. 2. Schematic of the CO_2 CARS instrument showing the location of the of the heterodyne detector in the detector room.

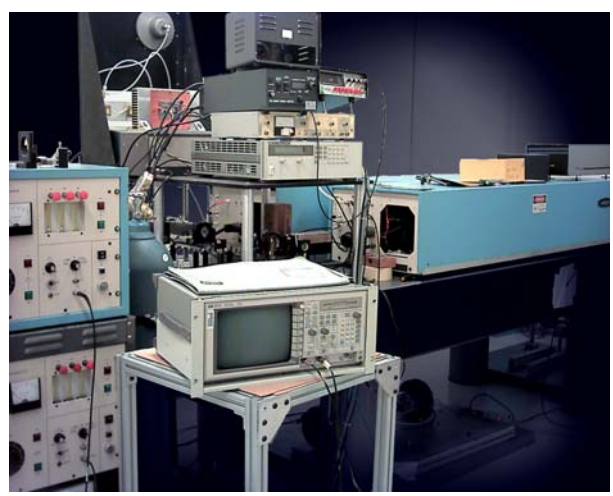

Fig. 3. CO_2 CARS instrument showing the location of the two pulsed lasers on the optic table and the optical path below the table with the sample cell.

laser of the two pulsed lasers was set to the 10P(18) laser line (at 10.57105 μm), and the lower-power pulsed laser was set to the 10P(20) line (at 10.59104 μm). These wavelengths were selected because they differ by 53GHz. The lasers energies were measured with a slow pyroelectric detector. The higher-power laser was adjusted to produce approximately 10 J, and the lower power laser was adjusted to 1 J. The lasers' pulse length was measured with a single-crystal germanium photon drag detector; both were found to produce a 100-ns-wide (FWHM) pulse. Therefore, the lasers produced pulses with 100 MW and 10 MW, respectively.

The nonlinear mixing was expected to produce a third beam at 10.5511 μm near the 10P(16) laser line which could be selected using the local oscillator laser. Unfortunately, the power supply for this local oscillator laser failed and prevented this measurement. To complete this measurement without a working local oscillator, a high- speed HgCdZnTe detector was set in the path approximately 1 m from the sample cell to detect the expected third beam. This detector was able to detect a signal coincident in time with the power from the pulsed lasers. The signal was not present when either pulsed laser was blocked, or when one was tuned to a different wavelength. With a calibration of the HgCdZnTe detector supplied by the manufacturer, and an estimate of the beam size at the detectors location, the power of this third beam was estimated at 3 W. To further check the probability that this third beam was produced by the nonlinear mixing of the two laser beams with D_2O, the sample was changed to H_2O and no signal from the third beam was observed.

Summary and Conclusions

The CO_2 CARS proof-of-principle instrument was constructed and demonstrated its capability in monitoring the presence of specific chemicals through the nonlinear four-wave mixing. With the addition of heterodyne detection, this technique holds the promise of extremely sensitive real-time sensing of complex chemicals. For the example with D_2O, the heterodyne sensitivity would allow detection at extremely low concentrations. In this proof-of-principle test, the D_2O concentration was 0.022 generating 3 W. With a heterodyne detection capability of less than 10^{-9} W,[2] D_2O can be monitored to concentrations below 10 parts per trillion.

- We have developed and demonstrated a new class of sensor for homeland security with proof-of-principle tests
- Unambiguous detection of chemicals in real time
- Detection is at 10 parts per trillion
- Instrument can built with off-the-shelf components
- Does not require the concentration of samples; ideal for direct sampling of airflow into buildings

Future efforts will involve producing a prototype sensor. This will be more compact than the sensor produced for this proof-of-principle test, possibly portable, and more versatile for wavelength tuning. Also, more complex chemicals will be investigated to verify the assumption that they will have distinct resonances accessible to the CO_2 CARS sensor with far greater sensitivity than 10 parts per trillion.

Future efforts may also enter into biological sampling. With the high-power lasers directly in the sample volume, biological specimens can be fragmented into chemical components for direct study. Identification of a specific biological agent would be through identification of several complex chemicals associated with this agent and the ratio of these chemicals.

For follow-on funding, a proposal has been submitted to Department of Homeland Security, and a proposal has is being drafted with the University of Tennessee for submission to the National Science Foundation.

References

[1]F. J. Lovas, J. S. Coursey, S. A. Kotochigova, J. Chang, K. Olson, and R. A. Dragoset, "Triatomic Spectral Database," National Institute of Standards and Technology on-line database <physics.nist.gov/PhysRefData/MolSpec/Triatomic/index.html>.

[2]R. K. Richards, D. P. Hutchinson, C. A. Bennett, H. T Hunter, and C. H. Ma, "Measurement of CO_2 Laser Small-Angle Thomson Scattering on a Magnetically Confined Plasma," *Appl. Phys. Lett.* **62**(1) 28–30 (1993).

Novel Platium Support for Proton-Exchange Membrane Fuel Cell Cathode and Anode Active Layer

T. J. Toops[1] and D.A. Blom[2]
[1]*Engineering Science and Technology Division*
[2]*Metals and Ceramics Division*

Fuel cells show great potential as a clean energy source for both mobile and stationary power, but considerable improvements are still necessary to reach this potential, primarily with respect to the cost/power ratio. This proposal details an alternative membrane construction for the proton-exchange membrane fuel cell (PEMFC) that may enable a 10-fold or greater reduction in the required platinum (Pt) mass, the most costly single component in the PEMFC. The key to this improvement comes from using a continuous array of aligned carbon nanotubules for the Pt support in the electrode. The aligned tubes constitute the active layer of the membrane assembly and will be tested against the current technology to quantify the improvement.

There is a growing interest in the development of alternative power sources in all areas of energy production. A field that has shown remarkable technological progress over the past 30 years is the fuel cell, particularly the proton-exchange membrane fuel cell (PEMFC).[1] Hurdles still exist in each step of this fuel-cell system, but one area that requires particular attention is the high cost of using Pt in the active layer of the anode and cathode. The chemical reactions necessary for fuel cells to generate power do not occur at the temperatures of interest (80–120°C) without a catalyst, and Pt is the most efficient catalyst for both the hydrogen oxidation reaction in the anode and the oxygen reduction reaction in the cathode; there are currently no known cost-effective alternatives to this noble metal. The current target for a competitive PEMFC is $45/kW by 2010, with an additional goal of $30/kW set for 2015. According to an Arthur D. Little study, the current cost of precious metals alone in the present day fuel cell is $65/kW, an estimated one-fifth of the total cost, which illustrates the necessity of marked improvement in this step.[2]

This project outlines a technique that will reduce the amount of platinum used in PEMFCs by at least an order of magnitude and significantly lower the cost of the fuel cell stack. This improvement is realized by minimizing the distance that H_2 and O_2 travel to the Pt catalyst and through the proton-exchange membrane. The current technology supports Pt on nanoporous carbon black in the electrode and requires the gas molecules to follow a long and tortuous path through the membrane electrode assembly (MEA) to reach the various reaction sites. The proposed Pt support is made of carbon nanochannels that enable the gas molecules to follow a linear path through the MEA to reach the various reaction sites. The inexpensive carbon nanochannels are easily formed in the pores of an aluminum oxide template, which are currently manufactured by several companies and are typically used in filtration processes. The nanochannels form an electrode that is essentially made of carbon nanotubes but without the high costs typically associated with nanotubes since the cost-prohibitive separation process is not necessary. These nanochannel-based electrodes could be used on both the anode and cathode of the MEA and would provide an optimum pathway for the reactants. This optimizes the use of Pt in the fuel cell and improves its efficiency and performance.

During FY 2003, we fully mapped the deposition rate of carbon on the walls of the alumina for both the small and large alumina templates and verified the rates with high-resolution transmission electron microscopy (HR-TEM) at ORNL's High Temperature Materials Laboratory (HTML). The HR-TEM also verified that there is no mass transfer limitation in the nominal 20-nm channels of the alumina template, as deposition was constant regardless of pore size (20–300 nm), that is, the channel thickness is constant throughout the membrane. Template removal has been executed for a wide array of carbon supports, and the method has undergone modifications to ensure the integrity of the nanotubular array. Platinum has been added to the nanotubular array after removal of the template, and particle size and deposition have been verified by HR-TEM. The channels before and after deposition are shown in Figs. 1 and 2, respectively. The tools and the materials to test both the current technology and the new electrode formulation have been acquired, with tests to commence shortly. A patent is pending based on the technology in

this project entitled "Integrated Membrane Electrode Assembly Using Aligned Carbon Nanotubules."

Improvements in the PEMFC is a key thrust to DOE's Office of Hydrogen, and this project fits directly into this area, which is the likely prime mover for FreedomCar. It is also relevant to the energy resources and the environmental quality missions of DOE. Many other federal agencies are investigating the usefulness of PEMFC, the primary barrier of which is high cost. If the research is successful in reducing the cost, multiple other federal agencies (Department of Defense, Department of Transportation, etc.) could benefit.

References

[1]P. Costamagna and S. Srinivasan, *J. Power Sources* **102**, 242 (2001) 242; P. Costamagna and S. Srinivasan, *J. Power Sources* **102**, 253 (2001).

[2]E. J. Carlson, J. Thijssen, S. Sriramulu, G. Stevens, and S. Lasher, *Cost Analysis o fFuel Cell Ssytem for Transportation*, final report, Ref 49739, SFAA No. DE-SCO2-98EE50526, Washington, D.C., Department of Energy (1998); http://www.fuelscells.org/adlittle2001.pdf

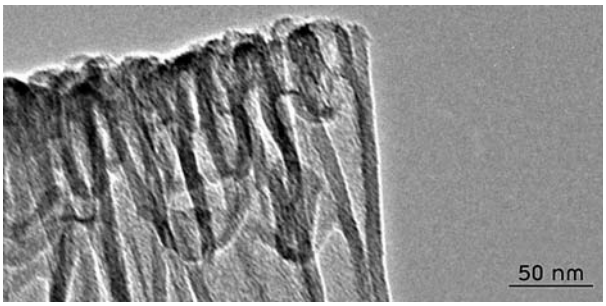

Fig. 1. HRTEM image of deposited carbon after removing the alumina template. Image illustrates aligned nanochannels of carbon with uniform wall thickness. Continuous array not possible to image at this scale due to thickness constraints of the microscope.

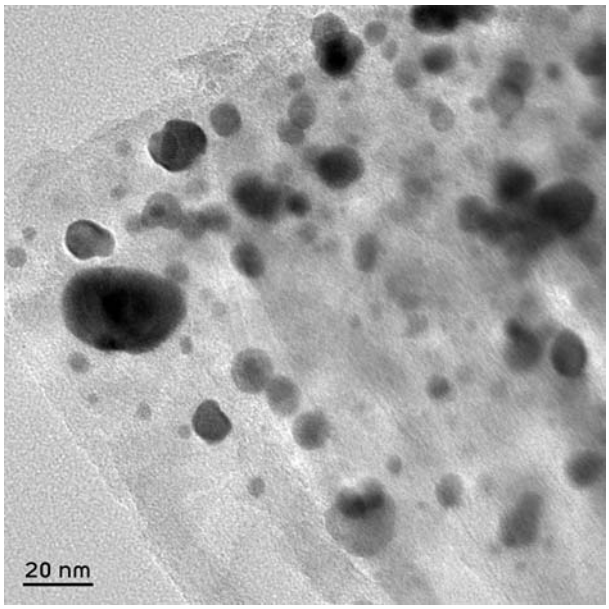

Fig. 2. HRTEM image of deposited carbon after removing the alumina template and depositing Pt.

Zero-Loss Fiber Optic Splitter

S. Rajic, P. G. Datskos, and W. R. Lawrence
Engineering Science and Technology Division

Development of a zero-loss fiber optic splitter would be an important technological advancement for the telecommunications industry. For instance, it would allow telecommunication providers to enable ancillary services to existing or additional customers at low cost. Such a development has proven to be elusive for previous researchers due to concerns about conservation of energy principles and associated signal amplification requirements. In fact, this view seems to be supported by numerous patents and open literature publications. All known prior approaches to signal splitting divert a small portion of the signal photons, usually by evanescent wave tunneling, to provide an additional information path for the original optical signal. When signal photons are removed, costly additional electronic amplifying repeater stations are needed to compensate for the diverted signal loss instead of simpler and less expensive optical repeaters. Thus, when considered for use in expanding service to new users on an existing transmission line, these techniques require expensive system modifications.

Our approach to splitting is a new concept for cascaded optical amplification involving only the inherent properties of the optical fiber. In this project, we intend to demonstrate proof-of-principle for the new technology while limiting the demonstration to only one channel of the 40-nm-wide telecom "C" band. To date, we have set up an experimental fiber-optic test system and collected initial coupling data. Additional work is under way to analyze the data and to optimize the system. Project plans are proceeding on schedule and within budget.

High-Speed Decay Lifetime Analysis Using Field-Programmable Gate Arrays

D. D. Earl
Engineering Science and Technology Division

Computing the lifetime of an exponentially rising or decaying signal is a common calculation associated with various noncontact measurement techniques. For a diverse range of sensing techniques (such as phosphor thermometry, molecular fluorescence lifetime spectroscopy, etc.), the speed at which this mathematical operation can be performed is often the key factor limiting a sensor's achievable measurement rate. Unfortunately, it is this limitation that prohibits decay-rate sensors from investigating and monitoring highly dynamic processes. The investigation of some of these dynamic processes (i.e., ultrafast surface heating/cooling, lattice energy exchange mapping, etc.) represents some of today's most exciting and promising research areas. Because of the varied analysis methods associated with decay-rate measurements and the low-volume demands of the average research consumer, a generalized user-configurable lifetime measurement digital signal processor (DSP) circuit suitable for laboratory use does not exist. The objective of this project is to develop the first DSP, written in VLSI Hardware Description Language, to realize high-speed, user-configurable, single-pulse lifetime measurements using field-programmable gate arrays.

Computing the lifetime of an exponentially rising or decaying signal is a common calculation associated with various measurement techniques. Phosphor thermometry, for example, accurately measures surface temperature by analyzing the fluorescent decay lifetime of certain temperature-sensitive phosphor coatings. Unfortunately, the mathematics associated with an exponential fit to real data can be computationally challenging, especially when signals exhibit a superposition of differing decay lifetimes. The speed at which this mathematical operation can be performed is often the key factor limiting a sensor's achievable real-time measurement rate. To provide the necessary computational power, without limiting data analysis options, a personal computer (PC)–based data acquisition system is typically the only feasible option for laboratory investigations. Unfortunately, the sluggish measurement rates of a PC-based system (<10 measurements/second) limits the decay-rate sensor to monitoring only slowly varying or static processes. With much of today's material research and sensor development involving highly dynamic processes, an improved data analysis platform is needed to enhance the applicability and potential of these unique sensing techniques.

The objective of this project is to develop a parameterized DSP algorithm, written in VLSI Hardware Description Language (VHDL), that can realize high-speed, user-configurable lifetime measurement circuitry in field-programmable gate arrays (FPGAs). FPGAs are re-configurable microcircuits that can be programmed (and reprogrammed multiple times) to realize complex digital circuit designs. Although FPGAs are generally slower than application-specific integrated circuits (ASICs), they can still provide significant hardware acceleration (1000–10000×) over PC-based systems while also permitting design modifications. The high computational speed and inherent design flexibility of an FPGA-based data analysis system makes it the ideal platform for enabling decay-rate sensors to investigate dynamic processes.

To date, we have written and simulated VHDL code to compute the lifetime of an exponentially decaying signal using three separate measurement algorithms. In tandem, an FPGA-based hardware prototype is being designed which allows signals from a photomultiplier tube (used to measure a decaying phosphor signal) to be converted into a digital signal accessible to an FPGA made by Altera Corporation and processed by this VHDL code. The prototype provides a hardware-user interface that allows various measurement values to be easily configured by the user, as well as a software interface that allows more sophisticated re-configuration of the hardware. The prototype is shown in Fig. 1. The prototype is still under construction and has not yet been tested on real-world signals. This testing is expected to start in late December 2003.

When completed, the FPGA-based data analysis prototype will enable ultrafast physical measurements previously considered impossible using decay-rate measurement techniques. This technology will have immediate applications to high-speed and two-dimensional phosphor thermometry research. ORNL researchers working on DOE's Freedom Car project have already expressed an immediate interest in using this device for

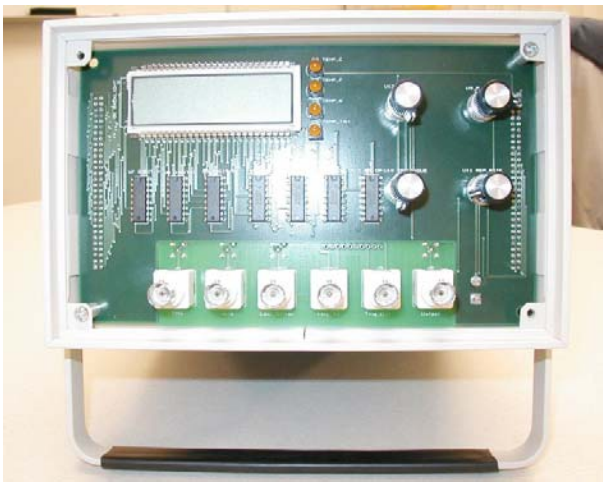

Fig. 1. FPGA-Based Decay Lifetime Measurement Prototype.

an upcoming field-test of phosphor thermometry sensors embedded in fuel cells.

The completed high-speed decay lifetime measurement system will be immediately applicable to thermographic phosphor research ongoing throughout the country. Specifically, it will be of immediate assistance to DOE projects related to the testing and development of fuel cells. Maximum efficiency operation of a fuel cell requires accurate knowledge of internal temperatures. Because of environmental considerations, these measurements are best made with a fiber-optic, phosphor thermometry sensor. Research at ORNL is already ongoing to develop these sensors for use in experimental fuel cell tests. Following the conclusion of this effort, the high-speed decay lifetime measurement system will be immediately applied to this research area as part of ORNL's contribution to DOE's Freedom Car program.

High Effective Hydrogen Storage Density

B. S. Richardson[1] and J. F. Birdwell[2]
[1]*Engineering Science and Technology Division*
[2]*Nuclear Science and Technology Division*

A significant barrier to the use of fuel cells for power generation in mobile and/or portable applications, particularly transportation, is the ability to store hydrogen at high density. A concept based on the release of chemically stored hydrogen by the catalytic hydrolysis of sodium borohydride using recycled water from the hydrolysis reaction excess and the oxidation of hydrogen in a proton exchange membrane (PEM) fuel cell (coupled to the reactor system) has the potential to exceed the DOE hydrogen storage density target. The objective of this research is to study and to demonstrate that sufficient water recovery and recycle can be achieved to sustain a continuous hydrolysis reaction with a significant reduction in the amount of required reagent water, thereby enabling a significant increase in storage density.

Mobile and portable power systems require high-density energy sources to operate efficiently. Increased interest in fuel cells as power sources for these types of applications, particularly automobiles, has resulted in the identification of high-density hydrogen storage technology as a critical need in the shift from hydrocarbons to hydrogen for transportation fuel. DOE has set target goals for hydrogen storage of 6 wt %, 1100 Wh/L, and 2 kWh/kg. While these targets have yet to be achieved, the automotive industry has stated a need for hydrogen storage at a minimum density of 12wt % as criteria for producing commercially viable hydrogen-powered vehicles.

One option for meeting the storage density target is to store hydrogen in a hydrolysable compound, couple the hydrolysis reaction with a fuel cell, and recycle excess hydrolysis water and fuel cell product water to the hydrolysis reaction. Sodium borohydride has several key characteristics that make it amenable for this approach. These include exothermic hydrolysis (to maximize net energy production), fast kinetics (facilitate hydrogen generation responsive to changing power demands), and hydrolysis only in the presence of a catalyst (for safety and controllability). In addition, the catalyzed hydrolysis is sufficiently exothermic to vaporize most of the excess water in the feed solution, facilitating separation of the water vapor from the $NaBO_2$ waste exiting the reaction chamber. Coupled with the fact that a fuel cell produces water as a by-product, it is theoretically possible to continuously segregate and recycle the water in a $NaBH_4$/fuel-cell system. In fact, since for every mole of water consumed in the hydrolysis reaction the reaction at the fuel cell produces two moles of water, the system is a potential net generator of water.

Water recycle eliminates the need for on-board storage of any significant volume of water, since solid $NaBH_4$ reactant can be dissolved on demand into a small volume of water that is continuously replenished during system operation. Consequently, the effective hydrogen storage density of the fuel to the system is 21 wt %: 10.5% from $NaBH_4$, which is doubled as a result of the H_2 contribution from recycled water.

This research effort was initiated in September of FY 2003, with this interim report covering startup activities performed in the last month of the fiscal year. We have conducted a more extensive literature search with regards to the properties of sodium borohydride and its hydrolysis. Of particular interest has been properties which would allow accurate real-time measurement of solution concentration. Potential catalysts have also been reviewed, with ruthenium shown to be an extremely effective catalyst for this reaction. Several ruthenium catalysts, on different substrate materials, shapes, and loadings, have been obtained for testing.

The current DOE hydrogen storage objectives are 6 wt %, with the automobile industry advocating a change in the target to 12 wt %. Thus there is the potential for significantly exceeding the DOE automotive industry targets with our approach. Upon demonstration of a proof-of-principle system, opportunities for follow-on funding within DOE and the commercial automotive industry will be pursued. In addition, this technology has potential application in a broad range of military applications. As this technology could be scaled, applications from unmanned air and ground systems, soldier-borne systems, and other portable systems could benefit from this research.